

Systematic Survey of Extended Lyman- α Sources Over $z \sim 3 - 5$ ¹

Tomoki Saito², Kazuhiro Shimasaku², Sadanori Okamura², Masami Ouchi^{3,4}, Masayuki Akiyama⁵, and Michitoshi Yoshida⁶

ABSTRACT

Spatially extended Ly α sources which are faint and compact in continuum are candidates for extremely young galaxies (age of $\lesssim 10^7$ yrs) at high redshifts. We carried out a systematic survey for extended Ly α sources, using deep intermediate-band imaging data taken with the Suprime-Cam on the Subaru Telescope. Our survey covers a field of view of $33' \times 25'$ and a redshift range of $3.24 \lesssim z \lesssim 4.95$, down to a Ly α flux of $\sim 1 \times 10^{-17}$ ergs cm $^{-2}$ s $^{-1}$. We identified 41 extended Ly α sources. The redshift distribution of these sources shows that this kind of objects are common in the early universe over the surveyed redshift range. The identified objects have typical sizes of $\sim 10 - 15$ kpc and luminosities of $\sim 10^{42}$ ergs s $^{-1}$. Follow-up spectroscopy made for 7 of the 41 objects showed that our sample suffers from little contamination. All 7 objects have large equivalent widths of Ly α emission line, all but one exceeding 240 Å in the rest frame. The large equivalent widths suggest that their extended Ly α emissions are unlikely to be due to normal starbursts, but possibly originated from very young galaxies. All 41 objects in our sample have much smaller Ly α luminosities than the two Ly α Blobs (LABs) found by Steidel et al. (2000) in spite of our much larger survey volume. This suggests that large and luminous extended Ly α objects like the two LABs are very rare and are clustered in overdense regions.

Subject headings: galaxies:formation — galaxies:high redshift

²Department of Astronomy, University of Tokyo, 7-3-1 Hongo, Bunkyo, Tokyo 113-0033, Japan

³Space Telescope Science Institute, 3700 San Martin Drive, Baltimore, MD 21210, USA

⁴Hubble Fellow

⁵Subaru Telescope, National Astronomical Observatory of Japan, 650 North A'ohoku Place, Hilo, HI 96720, USA

⁶Okayama Astrophysical Observatory, National Astronomical Observatory of Japan, 3037-5 Honjo, Kamogata, Okayama 719-0232, Japan

¹Based on data collected at the Subaru Telescope, which is operated by the National Astronomical Observatory of Japan.

1. Introduction

It has been said for a long time that galaxies undergoing their very first star formation must have strong Ly α line emission (Partridge & Peebles 1957). Recent large aperture telescopes have conducted many narrowband deep imaging surveys, which have successfully identified a large number of Ly α emitters (LAEs) at high redshifts (e.g. Cowie & Hu 1998; Hu et al. 1998; Fynbo et al. 2001; Rhoads et al. 2000; Ouchi et al. 2003; Shimasaku et al. 2003; Kodaira et al. 2003; Maier et al. 2003; Fynbo et al. 2003; Dawson et al. 2004). These LAEs show a relatively faint continuum and strong Ly α line emission. These surveys provide valuable information about very young galaxies, and therefore galaxy formation at high redshifts. However, it is not clear whether or not they are really young galaxies, i.e., under the initial phase ($\ll 10^7$ yrs) of their star formation. The LAEs found so far have substantial UV (rest frame) continua, though they are relatively faint. Hence they should already have a certain amount of stellar population. This means that most of the known LAEs are evolved galaxies. Some LAEs show extremely large equivalent widths, but they can be explained with ordinary starbursts by introducing a top-heavy IMF or zero-metallicity (Malhotra & Rhoads 2002).

It is known from many surveys that most of the high- z LAEs are relatively compact in Ly α emission (e.g. Pascarelle et al. 1998; Westra et al. 2005), although they are somewhat more extended in Ly α than in continuum (e.g. Møller & Warren 1998). On the other hand, galaxies in early phases ($\lesssim 10^7$ yrs) of their formation are predicted to have a spatially extended Ly α line emission originating from non-stellar mechanisms such as cooling radiation (Haiman et al. 2000; Fardal et al. 2001; Birnboim & Dekel 2003; Dekel & Birnboim 2006; Dijkstra et al. 2005a,b), resonant scattering of Ly α photons from central AGNs (Haiman & Rees 2001; Weidinger et al. 2004, 2005), or galactic superwinds driven by hidden starbursts (Taniguchi et al. 2001; Ohyama et al. 2003; Wilman et al. 2005), while they are fairly faint and/or compact in rest-frame UV continuum. Accordingly, we will be able to find extremely young galaxies by searching for *extended* Ly α sources which are faint and/or compact in continuum. The first distinctive example of such objects is the two Lyman- α Blobs (LABs) found at $z \sim 3.1$ by Steidel et al. (2000: hereafter S00). The two LABs received strong attention because of the unusual properties. Their strong Ly α emissions (Ly α luminosities of $\sim 10^{44}$ ergs s $^{-1}$) are more clearly extended than found by Møller & Warren (1998), with spatial extents of $\gtrsim 100h^{-1}$ kpc. Despite their extensive Ly α emission, they do not have detectable UV continuum sources sufficient to ionize the large amount of ambient H I gas. Although many observational studies ranging from radio to X-ray have been made (e.g. Chapman et al. 2001, 2004; Ohyama et al. 2003; Basu-Zych & Scharf 2004; Bower et al. 2004; Wilman et al. 2005), their nature is not yet clear.

It is also totally unknown how commonly extended Ly α sources exist at redshifts other than $z \sim 3.1$. There are only a restricted number of extended Ly α sources known to date (e.g. Keel et al. 1999; Francis et al. 2001; Dey et al. 2005; Nilsson et al. 2006). Currently the largest sample of extended Ly α sources is the sample of 35 objects by Matsuda et al. (2004: hereafter M04). More recently, Nilsson et al. (2006) made a narrowband imaging of a blank field (GOODS-S) and identified one object at $z = 3.16$ with extended Ly α emission and no detectable continuum counterparts. However, their samples are based on narrowband imaging which covers only small redshift ranges. M04’s survey is targeted at a particular overdense region including S00’s two LABs, and the redshift coverage is fairly small; $z = 3.09_{-0.03}^{+0.04}$. Nilsson et al. has yet smaller redshift coverage; $z = 3.157_{-0.031}^{+0.017}$. Thus, there is currently no systematic survey in a blank field which covers a wide range of redshift.

Our current work is aimed at searching for extended Ly α sources over a wide redshift range, by performing intermediate-band imaging. Since our intermediate-bands have wider bandwidths than usual narrowbands used for LAE surveys, we can cover a wider range of redshift. Although our survey sensitivity is restricted to strong emitters having large equivalent widths, extended Ly α sources with faint continuum like S00’s LABs have sufficiently large equivalent widths to be detected in our survey.

The rest of this paper is organized as follows. We introduce our imaging survey in §2.1, and the photometric selection of extended Ly α sources in §2.2. Then we describe the observational details of follow-up spectroscopy for the photometrically selected sample in §3. The photometric properties and spectral properties are presented in §4.1 and §4.2, and a discussion based on their luminosity function is presented in §4.3. Then we discuss currently proposed scenarios for extended Ly α sources in §4.4 using our imaging and spectroscopic data. We summarize our conclusions in §5.

Throughout this paper, we adopt cosmological parameters $\Omega_M = 0.3$, $\Omega_\Lambda = 0.7$, and $H_0 = 100h = 70 \text{ km s}^{-1} \text{Mpc}^{-1}$. All magnitudes are in the AB system (Oke 1974; Fukugita et al. 1995).

2. Photometric sample of extended Ly α sources

2.1. Intermediate-band imaging survey

We carried out a wide-field, deep imaging survey with the *Subaru Prime-focus Camera* (Suprime-Cam: Miyazaki et al. 2002) mounted on the 8.2m Subaru Telescope (Iye et al. 2004), using seven intermediate-band filters (IA filter system: Hayashino et al. 2000). The response curves of our filter set are shown in Fig.1. Each filter has a bandwidth of \sim

240 – 340Å giving $R = \lambda/\Delta\lambda \sim 23$. We can detect Ly α emission from almost the whole redshift range between $z = 3.24$ and $z = 4.95$ using these seven filters. The Suprime-Cam has a wide field of view, $34' \times 27'$ (central $33' \times 25'$ was used in this survey), so that our survey covers a large volume of $\sim 1 \times 10^6 h^{-3} \text{Mpc}^3$ in total. The observations were made on October 30 and 31 and November 6 in 2002 as an open-use program of the Subaru Telescope (S02B-163: Kodaira et al.). We pointed the telescope toward a blank-field called the Subaru/XMM-Newton Deep Field South (SXDF-S), which is located at $\alpha = 02^h 18^m 00^s$, $\delta = -05^\circ 25' 00''$ (J2000). Relevant data for the intermediate-bands are summarized in Table 1. The 3σ limiting magnitude ranges from 26.5 to 26.8 mag ($2''\phi$ circular aperture).

The SXDF-S has deep Suprime-Cam images in the B , R , i' , and z' bands. These broadband images were obtained in 2002 and 2003 in a large project of the Subaru Telescope named Subaru /XMM-Newton Deep Survey (SXDS: Sekiguchi et al. 2006). The exposure times and limiting magnitudes for the broadband images are also summarized in Table. 1. The 3σ limiting magnitudes in a $2''\phi$ circular aperture are 28.2 (B), 27.4 (R), 27.0 (i'), and 25.8 (z') mag, respectively. The response curves of these broadbands are also shown in Fig.1. Both the intermediate-band and broadband data were reduced with our own software tools based on NOAO IRAF software package. The photometric zero-points were calculated with ≥ 100 bright stars within the FoV of the Suprime-Cam, and corrected by amount of $\simeq 0.05$ mag to match their colors to those of galactic star spectra provided by Gunn & Stryker (1983). The seeing sizes ranged from $0''81$ (broadbands) to $1''.05$ (IA679 & IA709) in the raw images. All the images were smoothed with a Gaussian kernel to match their PSF sizes to the worst-seeing image ($1''.05$). After matching the PSF sizes, we performed source-extraction and photometry using SExtractor ver. 2.1.6 (Bertin & Arnouts 1996). We used the broadband data to measure continuum levels in selecting LAEs. Since the Suprime-Cam has a very wide FoV, our images have a few extremely bright stars and their ghost images. We carefully defined the regions affected by these stars and ghosts as well as a number of saturated stars, and did not use the sources extracted in these regions for further analysis. We also rejected the regions near the edge of the images. The regions rejected here make up $\sim 4.2\%$ of the whole area.

2.2. Photometric selection of extended Ly α sources

We have constructed a photometric sample of candidate extended Ly α sources from the intermediate (IA)-band and broadband imaging data. We measured the magnitude basically with a $2''\phi$ circular aperture unless otherwise noted. We selected candidates from objects brighter than 5σ in the IA-detection catalogues created with SExtractor. The outline of the

selection of extended Ly α sources is as follows. We first selected LAE candidates satisfying the following two criteria simultaneously: (1) the Ly α emission line has a sufficiently large equivalent width, and (2) non-detection or a large dropout in the B band. Then we further imposed the following two criteria on the sources selected with (1) and (2): (3) the spatial extent is significantly larger than point sources in the IA band, and (4) compact or faint in the continuum band red-ward of the Ly α line.

First, we selected objects of which the Ly α line has a sufficiently large equivalent width to be detected as IA-band excess relative to the broadband continuum strength. . The continuum levels to estimate equivalent widths (“Cont”) were measured with the broadband data red-ward of (and the closest to) the Ly α line, i.e., R -band for IA527 and IA574, i' -band for IA598, IA624, IA651, and IA679, and z' -band for IA709. We adopt the criterion of $\text{Cont} - \text{IA} > 0.75\text{mag}$, which corresponds to an observed-frame equivalent width $EW_{\text{obs}} \gtrsim 240\text{\AA} - 340\text{\AA}$ ($\gtrsim 55\text{\AA}$ in the rest-frame). Such large equivalent widths are rarely observed in foreground [O II] emitters, and the selected objects are likely to be Ly α emitters at high redshifts. In order to measure the total Ly α line flux, we used the IA magnitude measured with an automatic aperture (MAG_AUTO of SExtractor) in calculating the IA excess. On the other hand, we used the continuum magnitude measured with a $2''\phi$ circular aperture to minimize the effect of sky noise. This mixed use of different apertures enables us to effectively collect the Ly α line flux, and to measure the continuum level with a deeper limiting magnitude. Although this may increase contaminants due to its systematic overestimate of the IA excess, we can exclude contaminants with the fourth criterion, “compact or faint in continuum”, as described below.

Second, we selected from the IA-excess objects only those that were “drop out” or very faint ($< 2\sigma$) in the B band. This means that we selected objects with a large continuum gap between the B band and the continuum red-ward of the Ly α line. For the two bands corresponding to the lowest redshifts (IA527 and IA574), the expected continuum gap is not very large and hence objects with Lyman discontinuity can be detected even in the B band. Therefore, we used another criterion for these two bands: $B - R \geq 0.6$ for IA527, and $B - R \geq 1.4$ for IA574. Together with the first criterion, large IA-excess, we can expect that the selected sample of LAEs contains few low- z interlopers. These selection criteria are summarized in Table.2.

Then, we selected spatially extended Ly α sources from the LAE sample selected above. The spatial extent of Ly α line component was measured in the detected IA-band, and that of continuum component was measured in the broadband where we measured the continuum level for estimating the Ly α excess. The criterion we adopted for “extended” is $\text{FWHM}(\text{IA}) > 1''.4$, which means that the spatial extent of an object is larger than the PSF size ($1''.05$)

by more than $\simeq 2$ pixels ($0''.4$). As shown in Fig.2, we find that there are two kinds of objects among these “extended” Ly α sources. One is continuum-compact objects, that is, “objects which can be regarded as point-sources in continuum” (those in (a) in Fig.2), and the other is continuum-faint objects, that is, “objects which are too faint in continuum to reliably measure the FWHM in the continuum images” (those in (b) in Fig.2). We regarded an object as “continuum-compact” if it is brighter than the 3σ sky noise in the continuum band but its size is smaller than $1''.2$ (FWHM), and as “continuum-faint” if it is fainter than 3σ in the continuum band. Both groups are included in our sample because they all have extended strong Ly α emission. We selected 43 objects following these criteria; 23 continuum-compact objects and 20 continuum-faint objects. There are two double-counted objects, however, whose redshifts are covered by two IA bands; IA598-IA624, and IA651-IA679. After eliminating these two double counts, we finally obtained a sample of 41 extended Ly α sources. This sample includes 22 continuum-compact objects and 19 continuum-faint objects. The objects selected here are analogous to the two LABs of S00, but objects with smaller spatial extents are included because we adopted a smaller limiting size than the size of the LABs. The sky distribution of the 41 objects is shown in Fig.3.

The magnitudes and FWHM sizes of our objects selected above are listed in Table.3. As already mentioned, the magnitudes were measured basically with a $2''\phi$ circular aperture, but automatic aperture magnitudes (MAG_AUTO) were used for the IA band where Ly α emission was detected. The magnitudes in the IA band where Ly α line was detected and the nearest broadband red-ward of the Ly α line are written in bold characters in Table.3. Although we did not put any constraints on the continuum gap between the *B*-band and the red-ward broadband of Ly α for the bands redder than IA598, we found that all objects in our sample have fairly red *B* – Cont colors.

3. Follow-up spectroscopy

We carried out follow-up spectroscopy for seven objects among the 41 objects selected above. The observations were made on 2003 November 27, using *Faint Object Camera And Spectrograph* (FOCAS: Kashikawa et al. 2002) mounted on the Cassegrain focus of the Subaru Telescope. We used the multi-object spectroscopy (MOS) mode with three MOS masks, and obtained spectra of the seven candidate objects. The sky distribution of these MOS fields is also shown in Fig.3.

The 300B grism, the SY47 order-cut filter, and $0''.8$ -wide slits were used, giving a wavelength coverage of $\lambda \sim 4700 - 9100\text{\AA}$. This is sufficient to detect [O III] $\lambda\lambda 4959, 5007$ emissions in case the object is a foreground [O II] $\lambda 3727$ emitter. The spectral resolution of

this setting is $R \simeq 500$. This nominal resolution is equivalent to a wavelength resolution of $\simeq 12\text{\AA}$ at $\lambda = 6000\text{\AA}$, and a velocity resolution of $\simeq 600 \text{ km s}^{-1}$. The resolutions of spectra we finally obtained depend on the number of combined frames and the distance from the sky emission lines used for the references in the wavelength calibration. We measured the velocity width of the sky emission lines nearest to the Ly α line, and estimated the velocity resolutions to be $\sim 670 - 800 \text{ km s}^{-1}$. The exposure time for each mask was 1.5-2.5 hrs, giving an rms noise level of $\sim 10^{-19} \text{ ergs cm}^{-2} \text{ s}^{-1} \text{ \AA}^{-1}$ (25-26 mag).

The one-dimensional spectra of the seven objects are shown in Fig.4, and their spectral properties are summarized in Table 4. The wavelength range plotted in Fig.4 covers both the [O II] line and [O III] doublet lines in case the object is an [O II] emitter at redshift $0.38 \lesssim z \lesssim 0.94$. All of the spectra show only one strong emission line within the range of the detected IA bands except for spurious ones due to imperfect sky subtraction. None of them shows a detectable continuum emission down to $\sim 10^{-19} \text{ ergs cm}^{-2} \text{ s}^{-1} \text{ \AA}^{-1}$. We therefore conclude that all of them are single line objects, and that they all have large equivalent widths, as anticipated from the photometry. Similar results can be seen in the stacked spectrum shown in the bottom-right panel of Fig.4. Neither significant continuum emissions nor emission lines other than the candidate Ly α can be seen even in the stacked spectrum.

It is clear that three objects in our sample, IB08-86220, IB11-89537, and IB12-48320, do not have [O III] emission at the expected wavelength if the candidate Ly α line is in reality a foreground [O II]. If they are foreground [O II] emitters, there should be [O III] line emission detectable with our current spectral data. We therefore conclude that they are LAEs at high redshifts. For the rest of the sample, the spectra around the expected wavelength of the foreground [O III] lines are overlapped with sky emission lines. The emission lines detected in there are almost completely consistent with residuals of the known sky spectrum due to imperfect sky subtraction. Fig.5 shows the spectra around the candidate Ly α line. One object in our sample, IB12-81981, shows a marginal signature of an asymmetric line profile with a relatively sharp blue cut-off and a broader red wing, which are signatures of Ly α lines at high redshifts. The line profiles of the another two objects, IB11-89537 and IB12-48320, also show a marginal signature of asymmetry. It should be noted here that all seven objects have large equivalent widths of the candidate Ly α line. As described in §4.2, even the object with the smallest equivalent width, IB08-86220, has $EW_{rest} \sim 100\text{\AA}$ if the line is Ly α . If this is a foreground [O II] emitter at $z = 0.405$, the EW_{rest} is as large as 300\AA , which is hardly explained by an ordinary starburst galaxy.

By taking three pieces of observational information, detection of a single line, asymmetric line profile, and large equivalent width, we conclude that at least four objects, and probably all seven objects, are high- z Ly α emitters.

4. Results and discussion

4.1. Photometric properties

As seen in Table.3, all 41 extended Ly α sources of our sample are relatively faint in redward continuum. The spatial extents in continuum for 22 objects are clearly compact. The remaining 19 objects could be extended in continuum but their sizes are not measured reliably because they are too faint. The images of the seven objects observed spectroscopically are shown in Fig.6.

In order to estimate the true spatial extents, we made artificial images of PSF-smoothed exponential disks with various sizes and measured their FWHMs. We then established an empirical relation between the intrinsic half-light radii (HLR) of the exponential disk and the measured FWHMs of their PSF-smoothed artificial images. The HLRs of our objects were estimated using this FWHM-HLR relation. Although we do not know the precise radial profiles and shapes of our objects, exponential disks look a reasonable model. The left panel of Fig.7 shows the radial profile of a typical object in our sample, IB12-81981, together with the PSF-smoothed profile of a best-fit exponential disk. The distributions of FWHMs and calculated sizes ($2 \times$ HLR) are shown in Fig.8. Their typical sizes are $\sim 1''.5$ ($\sim 9.5 - 11$ kpc for surveyed redshifts) in FWHM, and their intrinsic HLRs calculated above are typically $\sim 0''.9$ ($\sim 5.7 - 6.8$ kpc). The physical size, defined as twice the HLR, is typically $\sim 1''.8$ ($\sim 11 - 14$ kpc). Strictly speaking, these values are spatial extents of both the Ly α line and continuum emission, because we did not subtract the continuum emission in measuring the FWHM. However, the FWHMs we obtained are almost solely determined from the extents of Ly α line emission because of their large equivalent widths.

The colors in Fig.8 represent detected IA bands, i.e., redshifts. They seem to be almost uniformly distributed over the surveyed redshift range $3.24 \lesssim z \lesssim 4.95$, showing that this kind of objects are common in the early universe. We did not detect any significant redshift dependence of their spatial extent. Their spatial extents are much smaller than those of S00's LABs which exceed ~ 100 kpc. The extent of the largest objects in our sample is $3''.2$ (~ 21 kpc) in FWHM and $2''.8$ (~ 19 kpc) in HLR. Because this object (IB13-104299) is, however, affected by a neighbouring bright object, we cannot obtain a reliable value of its physical size. The second largest object (IB11-3727) has an FWHM of $2''.5$ (~ 17 kpc) and an HLR of $2''.0$ (~ 14 kpc). Therefore, even the largest objects in our sample are extended less than ~ 30 kpc.

It is possible that the noise of the images causes systematic overestimates of the spatial extents of our objects. We stacked the images of the 41 objects, and investigated the radial profile. The right panel of Fig.7 shows the surface brightness on the stacked IA image as

a function of the radius. The radial profile shows that the stacked image is actually more extended than the PSF. We also stacked the red-ward continuum images of our objects, but found no clear signature that it is more extended than the PSF. We then examined how the noise of the observed images affects the apparent sizes of our objects by performing a Monte-Carlo simulation. Here we used the magnitude data of B band, IA-band (detection), and the broadband red-ward of Ly α line (continuum) shown in Table.3. The simulation procedure was as follows: (1) make 1025 artificial point-sources which have the same magnitude distribution as our sample, (2) add the Poisson noise, (3) put them randomly onto the original images, and (4) re-extract them with the same manner as for the observed data. These processes were repeated 100 times, and up to $\sim 90\%$ of the artificial objects are successfully re-extracted. We counted the re-extracted objects which satisfy our selection criteria presented in §2.2. Our simulation showed that $\sim 97\%$ of the re-extracted artificial objects (point sources) did not satisfy the selection criteria of our sample. This result shows that most of the objects in our sample are actually extended, and are not likely to be compact sources which are apparently extended due to noise.

Although most of our objects are really “extended” sources, we must note that our survey has a relatively low sensitivity to the Ly α line due to the wide bandpasses of the IA filters. This implies that we cannot detect low surface brightness components of Ly α emitting gas and that the sizes we obtained tend to be smaller than real. Moreover, because the distances of our objects are larger than that of S00’s LABs, the size distribution also suffers from cosmological dimming. For instance, when we detect LAB1/LAB2 with our surface-brightness thresholds, their sizes come down to $\sim 10''$ or less in the IA527 image, and $\sim 5''$ or less in the IA709. To estimate these effects in detail, we performed an imaging simulation, using the narrowband images of 35 LABs at $z \simeq 3.1$ provided by M04. The procedure of this imaging simulation is as follows.

We made simulated images of the LABs as if they were located at the redshifts covered by our survey and were observed through the same IA filters. First, we took the cosmological dimming effect into account. Next, we lowered the surface brightness of the simulated images by the amount corresponding to the ratio of the bandwidth of our IA filters to that of M04’s filter. Our IA filters have bandwidths of 240–340 \AA , while M04’s has 77 \AA . The surface brightness of the Ly α line emission was therefore lowered by a factor of 4–17 on the simulated images. Then we added noise to make the S/N ratios of the final simulated images equal to those of our observed IA images. We performed source extraction and photometry on the images with the same manner as for the observed IA images.

The simulated images for the LAB1 are shown in Fig.9, and the simulated size distribution of M04’s sample is shown in Fig.10. Even the most prominent object, S00’s LAB1,

gives a much smaller apparent size. For example, if it is located at $z = 4.82$ and observed through the IA709 filter, the measured FWHM will be $\sim 5''$ or so (~ 30 kpc). Similarly, if it is located at $z = 3.34$ and observed through the IA527 filter, the FWHM will be $\sim 10''$ (~ 70 kpc). Because its diffuse component becomes fainter than the sky fluctuation level, the apparent size of the extended emission itself becomes smaller, and the extended plateau emission is divided into two or more objects.

Similarly, we found that M04's objects are not much larger than the objects in our sample. Figs. 10 and 11 compare the sizes of our objects with those of M04's. While the M04 objects have much larger observed sizes (up to $\simeq 12''$) than our objects ($\lesssim 3''$), their sizes will decrease to $\lesssim 6''$ if they are observed through the IA filters under the same conditions as for our imaging. It should, however, be interesting to note that the average size of the “simulated” images of the M04 objects is slightly larger than that of our objects (see Fig. 10). The distribution of the simulated sizes of the M04 objects extends up to $6''$, while no object in our sample has a size larger than $4''$. This trend may suggest environmental dependence of extended Ly α emitting sources. The M04 objects reside in the highly overdense region in which S00's two large LABs are found. Overdense regions may include larger extended Ly α sources than normal fields. In fact, large objects like the two LABs have not been found in narrowband surveys. If such extended objects exist in our field, the surface brightness should be lower than the two LABs of S00.

4.2. Properties of the spectroscopic sample

We estimated the Ly α line fluxes, $F(\text{Ly}\alpha)$, of the objects in the spectroscopic sample from a combination of spectral and photometric data. The line fluxes directly obtained from the spectral data are smaller than the total $F(\text{Ly}\alpha)$ values, since we used $0''.8$ -wide slitlets. By making an artificial exponential disk image with the typical size of our objects, we calculated the typical fraction of the flux collected with a $0''.8$ -wide slit to be $\sim 40\%$ of the total flux.

In order to evaluate this fraction independently, we estimated the fraction using the broadband photometric data. First we assumed that the intrinsic UV continuum is flat within the detected IA band, and that this continuum level is equal to that of the redward continuum estimated from the broadband photometric data. Then we made a model flat-spectrum covering the IA band, and calculated the absorption of the IGM according to Madau (1995), using the redshift value obtained from the spectroscopy. The pure Ly α line flux was estimated simply by subtracting the absorption-corrected continuum flux from the total flux measured with the IA photometry. We compared this photometrically estimated

line flux (a) and the line flux measured simply by integrating the observed spectrum (b). The ratios (b)/(a) calculated for all seven objects in the spectroscopic sample ranged from 0.35 to 0.14, which is sufficiently smaller than the value for the artificial exponential disk, ~ 0.4 . Because we do not know accurate radial profiles and spatial extents, we adopted a conservative conversion factor (b)/(a)= 0.4 for all the objects in the spectroscopic sample in order to avoid overestimation of the Ly α line flux.

The rest-frame equivalent widths, EW_{rest} , were estimated from the line fluxes obtained above and the rest-frame UV continuum flux densities. The rest-frame UV continuum flux densities were estimated from the broadband photometric data red-ward of the detection IA band. The EW_{rest} 's before and after the correction for the collected flux are listed in Table.4. Fig.12 plots EW_{rest} (corrected) against line luminosities $L(\text{Ly}\alpha)$ (corrected). The errors are estimated by integrating the 1σ noise level of the spectra over the wavelength range where we measured the fluxes. Six out of the seven objects in our spectroscopic sample have large EW_{rest} values exceeding 240Å. The rest-frame Ly α equivalent width $EW_{rest} = 240\text{\AA}$ requires a top-heavy IMF of the slope $\alpha = 0.5$ or extremely young age ($\ll 10^7$ yrs), and thus $EW_{rest} = 240\text{\AA}$ is thought to be the upper limit for normal stellar populations (Malhotra & Rhoads 2002). The large equivalent widths of the objects in our spectroscopic sample indicate that they are unlikely to be normal starbursts like many other LAEs. Their EW_{rest} can be still larger, if we take into account the IGM absorption of the Ly α line itself. Moreover, because the six objects have continuum levels fainter than the 3σ of the broadband photometric data, our estimates of EW_{rest} give a lower limit.

We also measured the velocity width ΔV (FWHM) of the Ly α line. The ΔV value gives important information about their physical nature, because ΔV reflects the kinematical structure of the system. However, the profile of the Ly α line could not be significantly resolved for any of our objects. The measured nominal values are given in Table.4. All the objects have ΔV ranging from $\sim 600 \text{ km s}^{-1}$ to $\sim 800 \text{ km s}^{-1}$, which is comparable to the velocity resolutions. One object, IB11-59167, shows smaller ΔV than the estimated velocity resolution. However, this object is fairly faint, and located in the third MOS field where we took integration of only 1.5 hrs; the spectrum shows the peak S/N ratio of only ~ 2 , and the ΔV of this object is not reliable.

The velocity resolutions estimated from the line widths of the nearest sky emission lines are also shown in Table.4 in the parenthesis. These values give rough upper-limits of the intrinsic velocity widths, $\Delta V \sim 700 - 800 \text{ km s}^{-1}$. We can obtain somewhat stronger upper limits, using $\sqrt{(\Delta V + \text{Err}(\Delta V))^2 - (\text{resolution})^2}$, where $\text{Err}(\Delta V)$ is the observed error of the velocity width. The upper-limits thus estimated were $\simeq 300 - 800 \text{ km s}^{-1}$.

Although the upper-limits smaller than the velocity resolution are not very reliable, we

can infer from this result that our objects are unlikely to be prominent superwind galaxies, which have $\Delta V \gg 1000 \text{ km s}^{-1}$ (e.g. Heckman et al. 1991b). Our current resolutions and signal-to-noise ratios (S/N) are not high enough to study velocity structures.

4.3. Luminosity function

Our survey shows that extended Ly α sources are quite common in the early universe. We divided the number of objects detected (41) by our survey volume $\sim 1 \times 10^6 h^{-3} \text{ Mpc}^3$ (comoving) to obtain a number density of $\sim 4 \times 10^{-5} h^3 \text{ Mpc}^{-3}$. This value is lower than the number density, $\sim 4 \times 10^{-4} h^3 \text{ Mpc}^{-3}$, obtained from the two LABs and the survey volume of S00. We derived the luminosity function (LF) of the objects in our sample. Fig.13 shows the LF of our extended Ly α sources, down to the rest-frame surface brightness limits shown in Table 1. The surface-brightness limits correspond to luminosity limits of a few $\times 10^{42} \text{ ergs s}^{-1}$. Since we derived the LF from the raw number of our objects (no completeness-correction was made), the LF gives a lower limit of the number density.

The LF in Fig.13 shows that the number density per unit luminosity is $\sim 3 - 4 \times 10^{-5} h^3 \text{ Mpc}^{-3} / \Delta \log L(\text{Ly}\alpha)$ around $L(\text{Ly}\alpha) = 1 \times 10^{43} \text{ ergs s}^{-1}$, where $\Delta \log L(\text{Ly}\alpha) = 0.6020$. It decreases to $\sim 1 \times 10^{-5} h^3 \text{ Mpc}^{-3} / \Delta \log L(\text{Ly}\alpha)$ around $L(\text{Ly}\alpha) = 3 \times 10^{43} \text{ ergs s}^{-1}$. We also plot two data points to show an upper and lower limits of the LF (number density) of the two LABs of S00. The upper-limit of the number density was derived from the narrowband survey volume of S00, which is targeted to the redshift of the two LABs. The lower limit was derived from the volume surveyed for LBGs at $z \sim 3$ (Steidel et al. 2003). The survey area of Steidel et al. (2003) includes the S00's, but no such objects like the two LABs are found within their volume. The two brightest LABs have luminosities of $L(\text{Ly}\alpha) \sim 10^{44} \text{ ergs s}^{-1}$, which is brighter than our objects by an order of magnitude. However, their number density is comparable to that of our objects at $L(\text{Ly}\alpha) \simeq 10^{43} \text{ ergs s}^{-1}$.

Also plotted in Fig.13 are the LFs of the original M04 sample and simulated M04 sample. The latter was obtained with the imaging simulation based on the narrowband images of M04 described in §4.1. We performed source extraction for the seven simulated images with the same manner as our IA images. Then we merged the seven samples obtained, and calculated the number density by dividing the raw number of the objects by $7 \times$ (M04's survey volume). The number densities derived from the simulated M04 sample are, in general, higher than those of our objects by an order of magnitude. The LFs of the original and simulated M04 samples have a tail beyond $L(\text{Ly}\alpha) \simeq 5 \times 10^{43} \text{ ergs s}^{-1}$, while no object is found in our sample with such a high luminosity. There are no significant differences between the slopes of our LF and M04's at $2 \times 10^{42} - 2 \times 10^{43} \text{ ergs s}^{-1}$; both LFs are flat.

4.4. Possible physical origins of the extended Ly α emissions

Our extended Ly α sources have spatially extended strong Ly α emission with: (1) typical spatial extents of $\sim 10 - 15$ kpc, (2) typical Ly α line luminosities of \sim several $\times 10^{42} - 1 \times 10^{43}$, (3) large equivalent widths of $\sim 100 - 600$ Å, and (4) upper limits of the velocity widths of several $\times 10^2$ km s $^{-1}$. On the other hand, (5) they are very faint or compact in continuum emission.

We can infer possible origins of the extended Ly α emissions from these features. Currently proposed scenarios of extended Ly α emission are; (a) cooling radiation of infalling H I gas, (b) resonant scattering of Ly α photons from the central ionizing source by the surrounding H I gas envelope, or (c) shock-heating of the surrounding H I gas by superwind activity. We will discuss these scenarios using the features we found.

(a) Cooling radiation Haiman et al. (2000) and Fardal et al. (2001) predicted that primordial H I gas infalling into a dark matter halo would be shock-heated to emit an extended strong Ly α line detectable with current ground-based telescopes. In this case, Ly α photons are originated from infalling gas gravitationally heated to $\sim 10^4 K$. This process does not require UV continuum emission to produce Ly α emission. At a temperature of $\sim 10^4 K$, the Ly α line is the most effective cooling source, and it can release a large part of the gravitational energy. The Ly α line from infalling H I gas should therefore show a much larger equivalent width than that of a usual starburst, because there is no significant stellar population.

According to the simulation of Fardal et al. (2001), the cooling radiation cannot have a spatial extent as large as S00's LABs. The predicted spatial extent is consistent with that of our objects, $\sim 10 - 15$ kpc, suggesting that this picture possibly explains the extended Ly α emissions in our sample. The Ly α line luminosities $L(\text{Ly}\alpha)$ of our objects are also consistent with their prediction. The system with a Ly α cooling radiation brighter than 10^{43} erg s $^{-1}$ is expected to have high star formation activity, and hence $L(\text{Ly}\alpha)$ becomes larger than 10^{44} erg s $^{-1}$. The luminosity range of our objects is consistent with that of cooling-radiation-dominated systems. Their simulation also predicts that the velocity width cannot significantly exceed the circular velocity of the system, typically ~ 300 km s $^{-1}$ in half-width-half-maximum (~ 600 km s $^{-1}$ in FWHM), even if the effect of resonant scattering is taken into account. Our results of $\Delta V \lesssim 700 - 800$ km s $^{-1}$ (FWHM) therefore do not conflict with this picture. Since both the $L(\text{Ly}\alpha)$ and ΔV are scaled to the mass of the system, the correlation between $L(\text{Ly}\alpha)$ and ΔV should be a diagnostic of this scenario. However, our current spectral data do not have a sufficient quality, and this measurement should be done with future spectroscopy with a higher resolution and S/N ratio.

(b) Resonant scattering of Ly α photons The H I gas envelope surrounding an ionizing source can make the Ly α emission spatially extended by resonant scattering (Haiman et al. 2000). Ly α photons from the ionizing source is absorbed by surrounding H I gas, and re-emitted toward different directions. This process leads to a spatially extended Ly α emission. Since the spatial extents of our sample are only $\sim 10 - 15$ kpc, this reprocess by the H I gas surrounding the central starburst/AGN is a possible explanation.

If the ionizing source is an AGN, the observed large equivalent widths of the Ly α line can be easily explained. There is actually an extended Ly α source which is best explained by resonant scattering (Weidinger et al. 2004, 2005). For known Ly α nebulae associated with AGNs, however, the velocity widths are generally greater than ~ 1000 km s $^{-1}$ (van Ojik et al. 1997). The spatial extents of such nebulae are also larger than the objects in our sample in general ($\gtrsim 100$ kpc: Heckman et al. 1991a). Therefore, if the resonant scattering of AGN-originated Ly α photons is the case, our objects should be weak AGNs. Powerful AGNs are unlikely.

If the ionizing source is a starburst, on the other hand, their large equivalent widths require extreme cases. Malhotra & Rhoads (2002) showed that extremely young age ($\ll 10^7$ yrs) or top-heavy IMFs like $\alpha = 0.5$ can yield EW_{rest} values larger than 300Å. This suggests that the objects in our sample are unlikely to be normal starbursts. An extremely young stellar population may explain the observed large equivalent widths of our objects. In fact, most of the high- z LAEs can be understood as actively star-forming galaxies even if EW_{rest} is larger than 240Å (e.g. Wang et al. 2004). Another extreme case is that the continuum emission from the central starburst is obscured by dust. In this case, both the continuum and Ly α line should suffer from the absorption. However, if the surrounding gas envelope is spatially more extended than the compact starburst region, then the line emitter (gas) suffers from less absorption than the ionization source (starburst). Therefore, photo-ionization by starbursts is a possible explanation.

(c) Superwind For starburst-induced superwind galaxies known to date,

The measured velocity widths ΔV of starburst-induced superwind galaxies known to date range from several 100 km s $^{-1}$ to $\gtrsim 10^3$ km s $^{-1}$. Because upper-limits for our objects are $\Delta V \sim 700 - 800$ km s $^{-1}$, our objects are unlikely to be galaxies like known powerful superwinds. The spatial extents of our objects are also smaller than the typical powerful superwind source, Arp220, which has ionized gas extended up to several tens of kpc (Taniguchi et al. 1998).

However, we cannot rule out this scenario from our current data. The upper-limit of

$\Delta V \lesssim 800 \text{ km s}^{-1}$ for our sample could be consistent with superwinds with relatively small ΔV . There are two possible diagnostics of the superwind scenario. One is the velocity structure of the Ly α emission. If the Ly α nebula is shock-heated by the outflow activity of the galaxy, the Ly α line must show characteristic velocity structure of an expanding bubble. Another is the existence of C IV line emission. If the starburst-driven superwind is the origin of the extended Ly α emission, the primordial gas surrounding the system would be in some part chemically enriched. This enrichment would be detected as an extended C IV emission with a strength of typically 7–10% of the Ly α line (Heckman et al. 1991b). However, both diagnostics require spectra of a higher resolution and S/N ratio than our current data.

5. Conclusions

We have carried out a systematic survey for spatially extended Ly α sources which are faint and/or compact in rest-frame UV continuum, using seven intermediate-band images taken with Subaru/Suprime-Cam. We identified 41 objects in the redshift range of $3.24 \lesssim z \lesssim 4.95$. The lower limit of the number density was calculated to be $\sim 4 \times 10^{-5} h^3 \text{Mpc}^{-3}$ over a surveyed volume of $\sim 1 \times 10^6 h^{-3} \text{Mpc}^3$, down to $L(\text{Ly}\alpha) \sim 10^{42} \text{ ergs s}^{-1}$. These results show that this kind of extended Ly α sources are quite common in the early universe. A comparison of the luminosity function (LF) between our sample and M04’s showed that the number density of our objects is smaller than those of M04’s sample by an order of magnitude. No objects are found in our sample with luminosities as bright as \gtrsim several $\times 10^{43} \text{ ergs s}^{-1}$. This result shows that the largest and brightest objects like the two LABs of S00 are found only in highly overdense regions.

The Ly α line emission components of the objects in our sample have typical sizes of $\sim 10 - 15 \text{ kpc}$, and luminosities of several $\times 10^{42} \text{ ergs s}^{-1}$. Follow-up spectroscopy suggested that our sample suffers from little contamination. The objects in our sample have fairly large equivalent widths of Ly α line ($EW_{rest} \sim 100 - 600 \text{\AA}$). Six out of the seven objects with spectroscopy have $EW_{rest} \geq 240 \text{\AA}$; they cannot be normal starbursts. The ionizing source of the extended Ly α emission of our objects is likely to be either a non-stellar process of a forming galaxy, or a stellar UV radiation of an extremely young ($\ll 10^7$ yrs) or obscured starburst.

We thank Dr. Toru Yamada and Dr. Masanori Iye for their giving helpful advice and continuous support for preparing the manuscript. We thank Dr. Yuichi Matsuda for providing the narrowband imaging data, and giving us an important suggestion. We thank SXDS team for a fruitful discussion. We thank the anonymous referee for the valuable

comments which have greatly improved the paper.

REFERENCES

Basu-Zych A., Scharf C. 2004, ApJ, 615, L85

Bertin E., & Arnouts S. 1996, A&AS, 117, 393

Birnboim Y., & Dekel A. 2003, MNRAS, 345, 349

Bower R. G., et al. 2004, MNRAS, 351, 63

Cowie L. L., & Hu E. M. 1998, AJ, 115, 1319

Chapman S. C., Lewis G. F., Scott D., Richards E., Borys C., Steidel C. C., Adelberger K. L., & Shapley A. E. 2001, ApJ, 548, L17

Chapman S. C., Scott D., Windhorst R. A., Frayer D. T., Borys C., Lewis G. F., & Ivison R. J. 2004, ApJ, 606, 85

Charlot S., & Fall S. M. 1993, ApJ, 415, 580

Dawson S., Sprinrad H., Stern D., van Breugel W., de Vries W., & Reuland M. 2002, ApJ, 570, 92

Dawson S., et al. 2004, ApJ, 617, 707

Dekel A. & Birnboim Y. 2006, MNRAS, 368, 2

Dey A., et al. 2005, ApJ, 629, 654

Dijkstra M., Haiman Z., Spaans M. 2005, astro-ph/0510407

Dijkstra M., Haiman Z., Spaans M. 2005, astro-ph/0510409

Fardal M., Katz N., Gardner J. P., Hernquist L., Weinberg D. H., Romeel D., 2001, ApJ, 562, 605

Francis P. J., et al. 2001, ApJ, 554, 1001

Fukugita M., Shimasaku K., Ichikawa T. 1995, PASP, 107, 945

Fynbo J. U., Møller P., & Thomsen B. 2001, A&A, 374, 443

Fynbo J. P. U., Ledoux C., Møller P., Thomsen B., & Burud I. 2003, A&A, 407, 147

Gunn J. E., & Stryker L. L. 1983, ApJS, 52, 121

Haiman Z., Spaans M., & Quataert E. 2000, ApJ, 537, L5

Haiman Z., & Rees M. J. 2001, ApJ, 556, 87

Hayashino T., et al. 2000, Proc. SPIE, 4008, 397

Heckman T. M., Lehnert M. D., van Breugel W., & Miley G. K. 1991a, ApJ, 370, 78

Heckman T. M., Lehnert M. D., Miley G. K., & van Breugel W. 1991b, ApJ, 381, 373

Hu E. M., Cowie L. L., & McMahon R. G. 1998, ApJ, 502, L99

Iye M., et al. 2004, PASJ, 56, 381

Kashikawa N., et al. 2002, Proc. SPIE, 4008, 104

Keel W. C., Cohen S. H., Windhorst R. A., & Waddington I. 1999, AJ, 118, 2547

Kodaira K., et al. 2003, PASJ, 55, L17

Madau P. 1995, ApJ, 441, 18

Maier C., et al. 2003, A&A, 402, 79

Malhotra S., & Rhoads J. E. 2002, ApJ, 565, L71

Matsuda Y., et al. 2004, AJ, 128, 569 (M04)

Miyazaki S., et al. 2002, PASJ, 54, 833

Møller P., Warren S. J. 1998, MNRAS, 299, 661

Nilsson K., Fynbo J. P. U., Sommer-Larsen J., & Ledoux C. 2006, A&A Letters in press, astro-ph/0512396

Ohyama Y., et al. 2003, ApJ, 591, L9

Oke J. B. 1974, ApJS, 27, 21

Ouchi M., et al. 2003, ApJ, 582, 60

Partridge R. B. & Peebles P. J. E. 1957, ApJ, 148, 377

Pascarelle S. M., Windhorst R. A., & Keel W. C. 1998, AJ, 116, 2659

Rhoads J. E., Malhotra S., Dey A., Stern D., Spinrad H., & Jannuzi B. T. 2000, ApJ, 545, L85

Sekiguchi K., et al. 2006, in preparation

Shimasaku K., et al. 2003, ApJ, 586, L111

Steidel C., Adelberger K. L., Dickinson M., Giavalisco M., Pettini M., & Kellogg M. 1998, ApJ, 492, 428

Steidel C., Adelberger K. T., Shapley A. E., Pettini M., Dickinson M., & Giavalisco M. 2000, ApJ, 532, 170 (S00)

Steidel C., Adelberger K. L., Shapley A. E., Pettini M., Dickinson M., & Giavalisco M. 2003, ApJ, 592, 728

Taniguchi Y., Trentham N., & Shioya Y. 1998, ApJ, 504, L79

Taniguchi Y., & Shioya Y. 2000, ApJ, 532, L13

Taniguchi Y., Shioya Y., & Kakazu Y. 2001, ApJ, 562, L15

van Ojik R., Röttgering H. J. A., Miley G. K., & Hunstead R. W. 1997, A&A, 317, 358

Wang J. X., et al. 200, ApJ, 608, L21

Weidinger M., Møller P., & Fynbo J. P. U. 2004, Nature, 430, 999

Weidinger M., Møller P., Fynbo J. P. U., & Thomsen B. 2005, A&A, 436, 825

Westra E., Jones D. H., Lidman C. E., Athreya R. M., Meisenheimer K., Wolf C., Szeifert T., Pompei E., & Vanzi L. 2005, A&A, 430, L21

Wilman R. J., Gerssen J., Bower R. G., Morris S. L., Bacon R., de Zeeuw P. T., & Davies R. L. 2005, Nature, 436, 227

Table 1. Summary of the imaging data

Band	Exposure [sec]	$m_{\text{lim}}(3\sigma)^{\text{a}}$ [mag]	$\Sigma_{\text{lim}}(2\sigma)^{\text{b}}$ [ergs cm $^{-2}$ s $^{-1}$ arcsec $^{-2}$]	$N(> 3\sigma)^{\text{c}}$	Redshift of Ly α
IA527	5280	26.8	1.27×10^{-15}	67405	3.34 ± 0.10
IA574	7200	26.5	2.37×10^{-15}	57824	3.72 ± 0.11
IA598	6720	26.5	2.80×10^{-15}	60219	3.93 ± 0.12
IA624	10560	26.7	2.56×10^{-15}	69571	4.12 ± 0.12
IA651	6500	26.7	2.76×10^{-15}	71365	4.35 ± 0.13
IA679	10560	26.8	3.11×10^{-15}	70228	4.58 ± 0.14
IA709	11520	26.6	3.86×10^{-15}	68535	4.82 ± 0.13
<i>B</i>	18000	28.2	—	115354	—
<i>R</i>	12000	27.4	—	95230	—
<i>i'</i>	13200	27.0	—	85198	—
<i>z'</i>	5700	25.8	—	51599	—

^aThe 3- σ limiting magnitude measured with a $2''\phi$ circular aperture.

^bThe threshold of the source extraction in rest-frame surface brightness of the Ly α line.

^cThe number of objects brighter than 3σ .

Table 2. Color selection criteria of Ly α sources

Detected band (Ly α)	Ly α -excess (Cont)	<i>B</i> -nondetection or dropout
IA527	<i>R</i>	$R - \text{MAG_AUTO}(\text{IA527}) > 0.75$
IA574	<i>R</i>	$R - \text{MAG_AUTO}(\text{IA574}) > 0.75$
IA598	<i>i'</i>	$i' - \text{MAG_AUTO}(\text{IA598}) > 0.75$
IA624	<i>i'</i>	$i' - \text{MAG_AUTO}(\text{IA624}) > 0.75$
IA651	<i>i'</i>	$i' - \text{MAG_AUTO}(\text{IA651}) > 0.75$
IA679	<i>i'</i>	$i' - \text{MAG_AUTO}(\text{IA679}) > 0.75$
IA709	<i>z'</i>	$z' - \text{MAG_AUTO}(\text{IA709}) > 0.75$

Note. — The second column (Cont) means the band where we measure the continuum levels, i.e. the nearest red-ward broadband of the Ly α line. Magnitudes are measured with a $2''\phi$ aperture unless otherwise noted. The criteria for spatial extent are common for all the IA bands; $\text{FWHM}(\text{IA}) > 1''.4$ and $\text{FWHM}(\text{Cont}) < 1''.2$.

Table 3. Photometric properties of extended Ly α sources

Object ID	α (J2000)	δ (J2000)	<i>B</i>	<i>R</i>	<i>i'</i>	<i>z'</i>	IA527	IA574	IA598	IA624	IA651	IA679	IA709	auto (IA)	FWHM [$''$] (IA)	FWHM [$''$] (Cont)
IB08-2031	2:17:56.66	-5:37:47.7	28.21	27.45	27.41	27.00	25.83	27.70	27.56	27.90	26.71	27.64	27.80	25.24	1.71	1.46
IB08-20047	2:18:43.50	-5:33:48.0	27.06	26.36	26.33	26.11	25.93	27.17	26.81	26.18	26.17	26.59	26.49	25.21	2.15	1.14
IB08-27691	2:18:59.40	-5:31:58.8	29.40	28.15	27.47	27.00	25.77	27.70	27.52	27.90	27.82	27.24	27.53	25.65	1.42	0.93
IB08-28421	2:18:20.07	-5:31:49.9	27.32	26.45	26.50	27.00	25.94	26.88	26.89	26.89	26.81	26.82	26.34	25.62	1.48	1.09
IB08-36255	2:17:20.80	-5:29:58.6	26.59	25.85	25.87	25.69	25.58	26.16	26.11	26.03	25.90	25.89	25.70	24.73	1.55	1.16
IB08-86220	2:18:28.32	-5:18:11.9	27.20	26.51	26.48	27.00	25.76	26.40	26.72	26.43	26.68	27.20	27.10	25.40	1.63	1.20
IB10-17108	2:16:58.03	-5:34:19.1	27.16	25.65	25.65	25.72	26.63	25.07	25.49	25.75	25.63	25.84	25.74	24.83	1.41	1.09
IB10-17580	2:18:29.03	-5:34:08.8	28.19	26.39	26.28	25.95	28.00	25.76	27.09	27.13	26.62	27.10	26.65	25.28	2.15	1.16
IB10-32162	2:16:56.88	-5:30:29.5	27.53	25.98	26.30	26.14	26.85	25.22	25.73	26.00	26.12	26.14	26.17	24.90	1.68	1.14
IB10-54185	2:17:59.46	-5:25:07.2	28.16	26.44	26.42	26.61	27.31	25.61	25.98	26.55	26.42	26.59	26.26	25.13	1.46	1.08
IB10-79754	2:19:02.00	-5:18:54.7	29.40	28.60	28.20	26.46	28.00	25.94	27.70	27.90	27.90	28.00	27.36	25.87	1.48	2.09
IB10-90651	2:17:43.32	-5:16:12.0	29.40	27.75	27.79	27.00	26.96	25.84	27.23	27.90	27.90	27.39	26.66	25.50	2.42	2.87
IB11-3727	2:19:06.14	-5:37:29.1	29.40	28.60	28.20	27.00	28.00	27.51	25.94	27.90	27.55	28.00	27.80	26.04	2.47	0.00
IB11-5427	2:18:30.81	-5:37:10.7	29.37	26.16	26.61	27.00	26.66	27.70	25.86	25.76	26.16	26.93	26.29	25.62	1.49	1.18
IB11-6145	2:16:53.46	-5:36:58.8	29.40	26.36	27.17	26.65	27.12	27.70	25.63	26.21	27.46	26.99	27.80	25.28	2.27	1.38
IB11-59167	2:17:10.19	-5:23:47.2	29.40	26.71	27.59	27.00	27.43	26.92	25.80	27.90	27.77	27.63	27.37	25.54	2.08	2.29
IB11-66309	2:18:36.55	-5:21:52.3	29.40	26.62	26.92	27.00	27.32	27.68	25.77	26.54	26.95	27.02	27.80	25.60	1.92	1.10
IB11-80344	2:17:44.67	-5:18:15.0	29.08	26.70	27.03	26.95	28.00	27.59	25.53	26.85	27.29	26.75	26.96	25.24	2.07	1.88
IB11-89537	2:17:45.31	-5:15:53.2	29.40	26.65	27.25	27.00	28.00	27.70	25.80	25.58	27.90	27.49	27.70	25.52	1.49	1.23
IB11-101786	2:17:47.30	-5:13:05.2	29.40	27.22	27.01	26.39	28.00	27.70	25.97	27.90	27.68	28.00	27.80	25.92	1.73	2.12
IB12-1092	2:19:06.27	-5:37:53.3	29.40	26.71	26.52	27.00	27.00	27.70	26.28	25.81	26.16	26.90	26.60	25.66	1.86	1.14
IB12-21989	2:17:13.33	-5:32:56.5	29.40	25.12	25.88	25.72	28.00	27.48	26.66	25.71	26.47	26.15	26.02	25.06	1.48	1.13
IB12-30834	2:17:55.95	-5:30:53.2	29.40	27.10	27.09	27.00	28.00	27.70	27.70	25.82	27.84	27.76	27.80	25.71	1.47	1.11
IB12-48320	2:16:55.87	-5:26:36.9	29.07	26.59	27.35	25.82	28.00	27.70	26.05	25.82	27.90	26.82	27.56	25.35	1.61	2.53
IB12-58572	2:17:49.08	-5:24:11.4	29.40	27.16	26.82	27.00	26.87	27.70	26.52	25.97	26.84	26.64	27.34	25.32	1.57	1.17
IB12-71781	2:17:38.93	-5:20:57.8	29.16	26.68	26.77	26.71	27.79	27.70	26.89	25.96	27.32	27.34	26.49	25.67	1.55	1.15
IB12-81981	2:18:14.69	-5:18:32.2	29.40	26.85	27.84	27.00	26.88	27.70	27.70	25.65	26.87	26.79	27.62	25.27	1.77	2.80
IB13-999	2:18:56.49	-5:37:54.6	29.24	27.42	28.20	27.00	27.76	27.70	27.70	27.90	25.98	28.00	27.80	25.87	2.00	2.34
IB13-20748	2:18:41.91	-5:33:19.4	29.40	26.57	27.21	26.30	28.00	27.54	27.70	27.90	25.60	26.47	27.30	25.20	1.58	2.00
IB13-28369	2:18:39.14	-5:31:26.7	29.40	26.70	27.49	27.00	28.00	27.70	27.52	27.34	25.59	27.61	27.80	24.98	1.61	2.48
IB13-62009	2:17:28.52	-5:23:17.5	29.40	26.83	27.08	27.00	27.16	27.32	27.36	26.24	25.95	27.77	27.44	25.53	2.23	2.85
IB13-95072	2:17:00.33	-5:15:19.2	29.40	26.77	27.26	27.00	28.00	27.70	27.70	27.90	25.49	28.00	27.80	25.31	1.44	1.86
IB13-96047	2:18:13.30	-5:15:05.0	29.40	26.16	25.97	25.85	28.00	26.99	27.65	27.90	25.80	25.85	26.04	25.16	1.54	1.18
IB13-104299	2:18:21.06	-5:13:24.8	29.17	26.56	27.45	26.71	28.00	26.62	27.70	27.90	25.87	26.78	26.19	25.48	3.15	3.15
IB14-47257	2:18:01.94	-5:25:25.0	29.40	26.62	26.29	26.65	28.00	27.56	27.11	27.54	27.54	25.93	26.44	25.14	1.44	1.19
IB14-52102	2:18:00.10	-5:24:10.3	29.40	26.21	26.33	26.06	27.54	26.67	26.78	27.03	26.01	25.39	25.83	25.15	1.43	1.11

Table 3—Continued

Object ID	α (J2000)		δ		<i>B</i>	<i>R</i>	<i>i'</i>	<i>z'</i>	IA527			IA574			IA598			IA624			IA651			IA679			IA709			auto		FWHM [$''$]	
	α	δ	α	δ					IA527	IA574	IA598	IA624	IA651	IA679	IA709	(IA)	(IA)	(Cont)															
IB14-62116	2:17:58.21	-5:21:35.4	28.82	26.08	25.88	26.09	28.00	27.70	26.57	27.69	27.90	25.14	26.09	24.74	1.50	1.14																	
IB15-66451	2:18:33.92	-5:22:09.3	29.40	26.47	25.70	25.87	28.00	27.70	27.70	27.35	27.71	28.00	25.23	24.79	1.58	1.58																	
IB15-94328	2:16:55.31	-5:15:22.0	29.17	26.85	25.73	25.95	28.00	27.70	27.70	27.24	27.22	27.23	25.27	25.09	1.52	2.40																	

Note. — Magnitudes were measured with a $2''\phi$ circular aperture, except the column “auto”. For objects fainter than the 1σ flux limit, the 1σ limiting magnitudes are shown instead of the SExtractor’s outputs. The “auto” column shows MAG_AUTO measured in the detected IA band (i.e. Ly α line). The FWHM means the spatial extent in FWHM measured on the image (in arcsec). The (IA) is for the detected IA band, and (Cont) is for the red-ward continuum band. The magnitudes in the red-ward continuum band and the detected IA band are written in bold characters. The α and δ are the right ascension and declination (J2000) based on the beta-version astrometry given in the SXDS broadband data.

Table 4. Spectral properties of extended Ly α sources

Object ID	λ_c^a [Å]	z	$F(\text{Ly}\alpha)^b$ [ergs cm $^{-2}$ s $^{-1}$]	$L(\text{Ly}\alpha)^b$ [ergs s $^{-1}$]	EW_{rest}^b [Å]	ΔV (resolution) c [km s $^{-1}$]	ΔV_{upper}^d [km s $^{-1}$]
IB08-86220	5235	3.31	$1.2 \pm 0.6 (3.0) \times 10^{-17}$	$1.2(3.0) \times 10^{42}$	44 (110)	748 (750)	550
IB10-90651	5692	3.68	$1.6 \pm 0.5 (4.0) \times 10^{-17}$	$2.0(5.0) \times 10^{42}$	164 (410)	795 (740)	440
IB11-59167	6005	3.94	$8.6 \pm 7 (22) \times 10^{-18}$	$1.3(3.2) \times 10^{42}$	75 (188)	627 (700)	300
IB11-80344	5943	3.89	$2.6 \pm 0.6 (6.5) \times 10^{-17}$	$3.8(9.5) \times 10^{42}$	156 (390)	795 (780)	770
IB11-89537	6110	4.02	$2.1 \pm 0.4 (5.2) \times 10^{-17}$	$3.2(8.0) \times 10^{42}$	136 (340)	779 (780)	550
IB12-48320	6123	4.04	$1.6 \pm 0.5 (4.0) \times 10^{-17}$	$2.6(6.5) \times 10^{42}$	132 (330)	695 (700)	450
IB12-81981	6225	4.12	$1.6 \pm 0.5 (4.0) \times 10^{-17}$	$2.7(6.8) \times 10^{42}$	179 (448)	789 (670)	680

^awavelength of the line center.

^b Indicated in the parenthesis is the value corrected for the flux loss with the 0''.8-wide slit.

^cVelocity resolutions are shown in the parentheses.

^dUpper limits of the velocity widths.

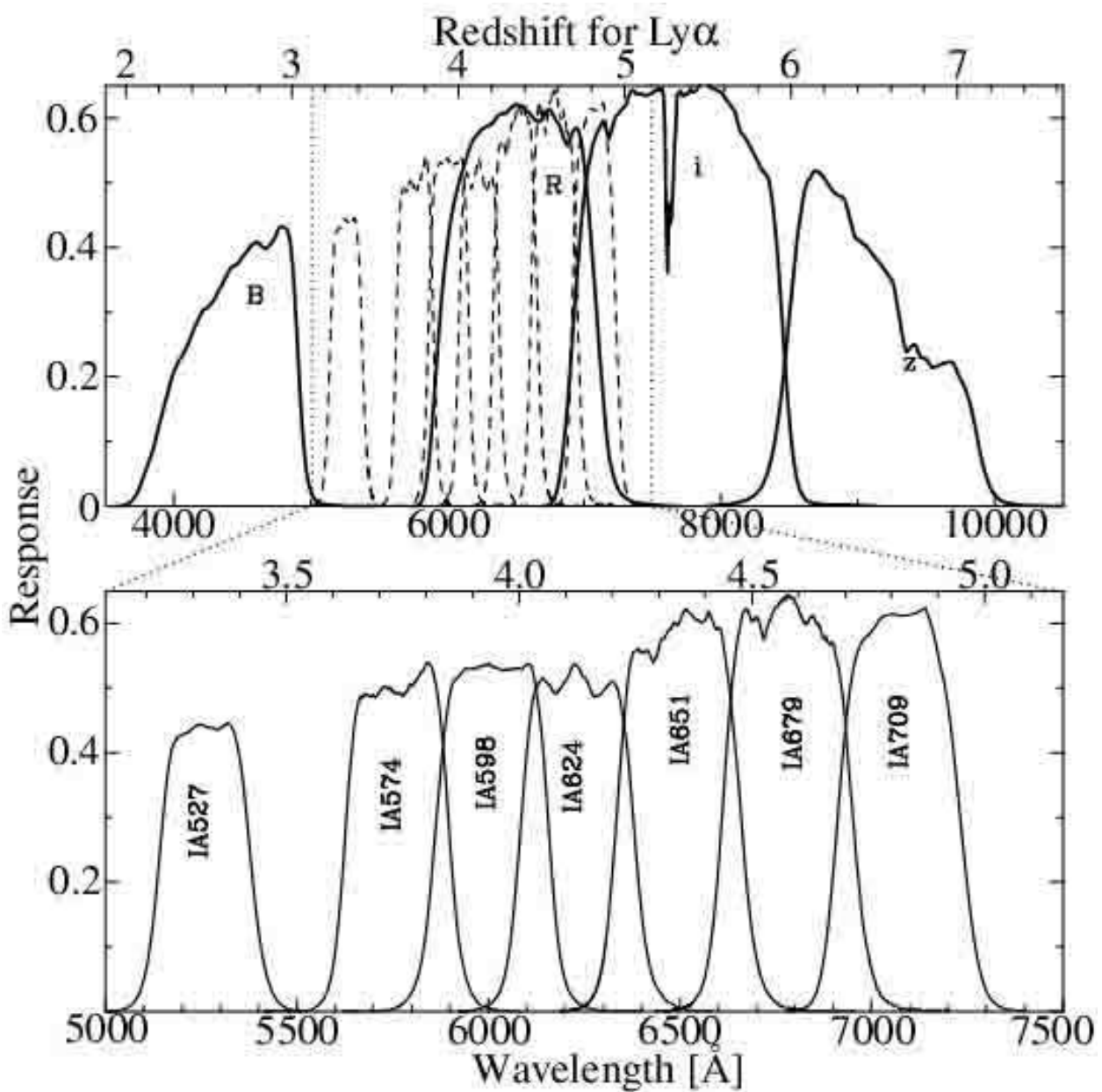


Fig. 1.— The upper panel shows the responses of the filters used in our survey. The dashed curves represents the seven intermediate-band (IA) filters, and the solid curves represent the four broad-band filters. The lower panel is a zoom up for the IA filters. The abscissa represents the wavelength (marked on the bottom) and the redshift for the Ly α line (marked on the top).

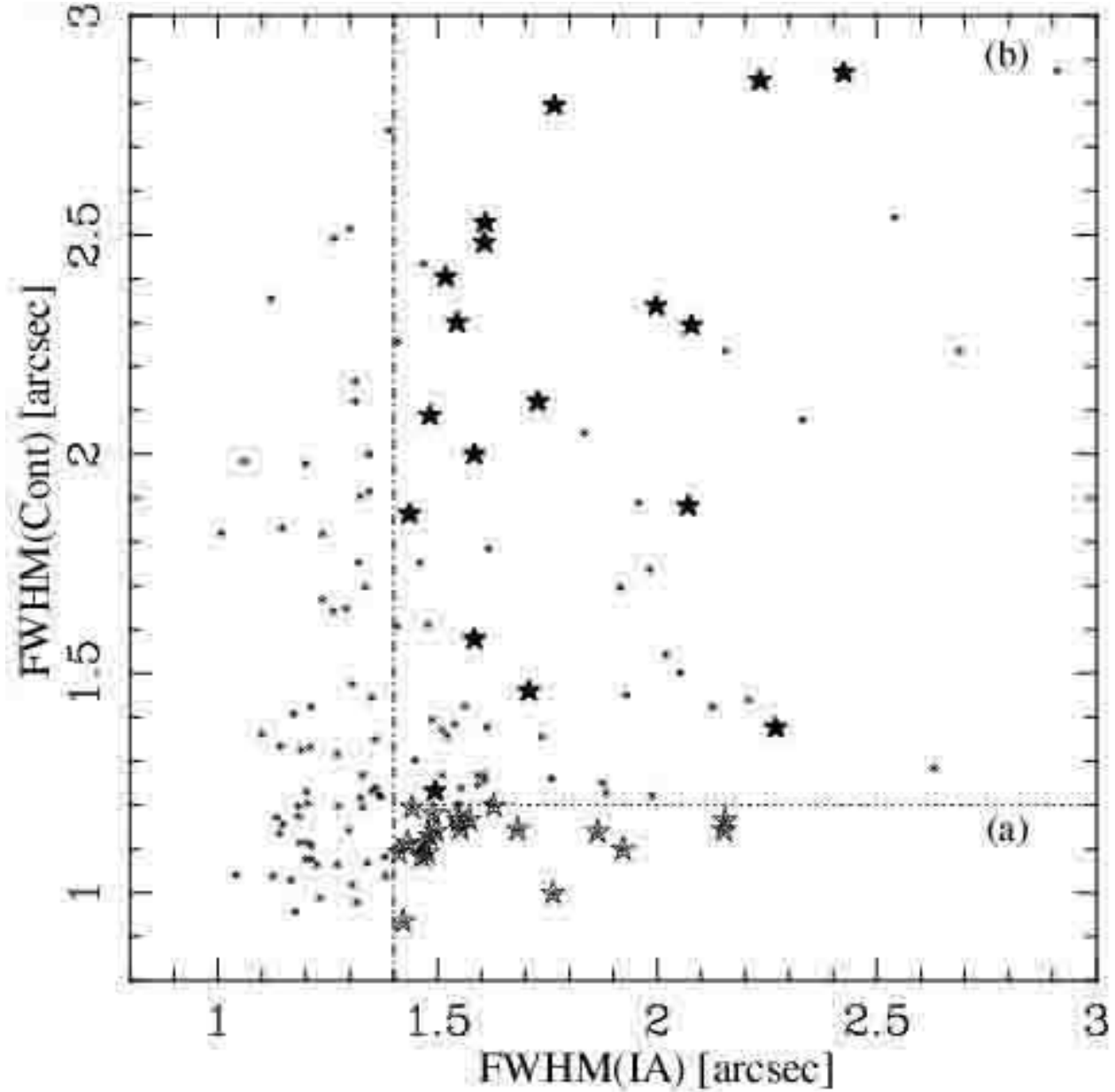


Fig. 2.— Size distribution of the photometrically selected extended Ly α source candidates in the IA and continuum bands. The abscissa shows FWHM in the detected IA band, and the ordinate shows FWHM in the continuum band red-ward of the Ly α line. The asterisks indicate all objects satisfying the criteria of Ly α excess and B -band non-detection/dropout. The star marks represent our sample of extended Ly α sources. The open stars in region (a) are continuum-compact objects. The filled stars in region (b) are continuum-faint objects, which are too faint in continuum to have the sizes measured with a reasonable accuracy, i.e., the abscissa values for these objects are not reliable (see the text). The threshold for the spatial extent in Ly α is shown with the vertical dot-dashed line, and that in continuum is shown with the horizontal dotted line.

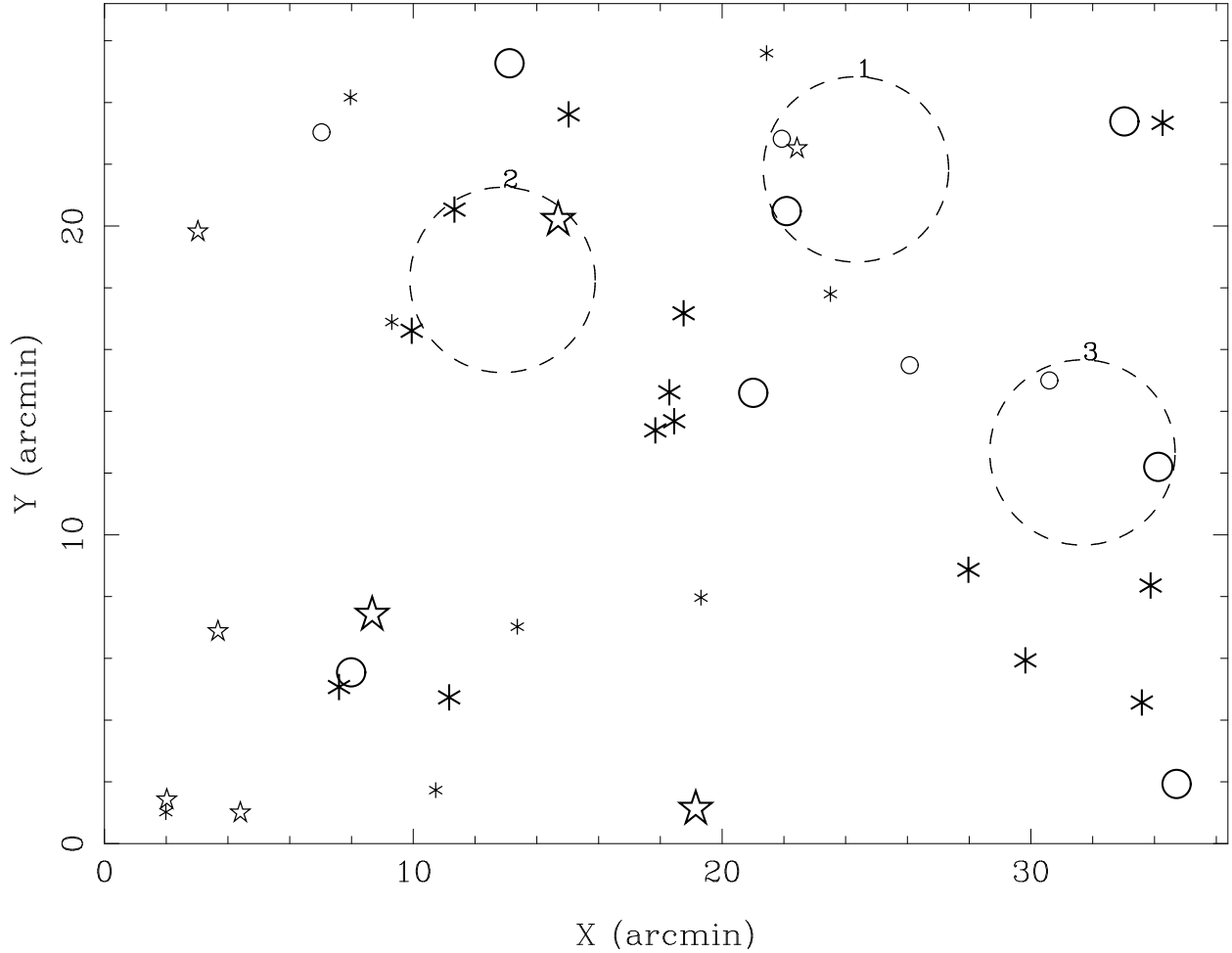


Fig. 3.— Sky distribution of extended Ly α source candidates in our sample. The dashed circles indicate the three MOS FoVs of follow-up spectroscopy. Spectra were obtained for 7 of the 41 candidates. The open stars and open circles indicate objects with a large Ly α excess: $\text{Cont} - \text{IA} > 2.5$ and $\text{Cont} - \text{IA} > 1.5$, respectively, where the Cont is the continuum magnitude measured in the broadband red-ward of the Ly α line. Objects marked with large symbols are brighter than 25.5 mag in the IA band.

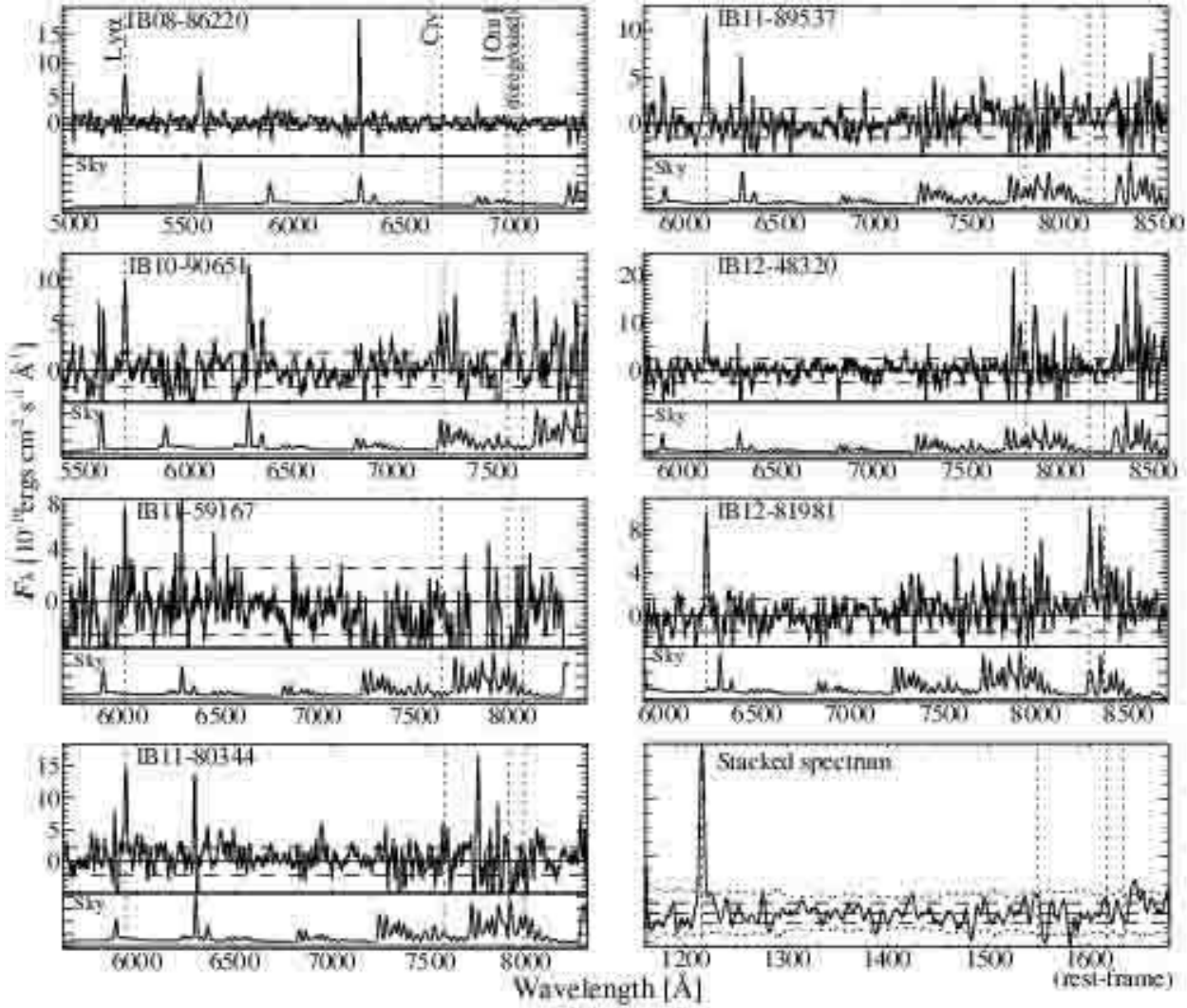


Fig. 4.— One-dimensional spectra of the seven extended Ly α sources, integrated over the full extents along the slit direction. The wavelength ranges plotted here are $1150 \leq \lambda/(1+z) \leq 1700\text{\AA}$. The wavelengths of Ly α , C IV, and foreground [O III] are marked with the vertical dotted lines. The horizontal dashed lines are $\pm 1\sigma$ noise levels calculated from the whole spectral range plotted here. The sky spectrum is plotted at the bottom of each panel. All the wavelengths are in the observed-frame, except for the stacked spectrum shown in the bottom-right panel. For the stacked spectrum, the dotted curves show $\pm 1\sigma$ noise levels calculated from the photon counting errors.

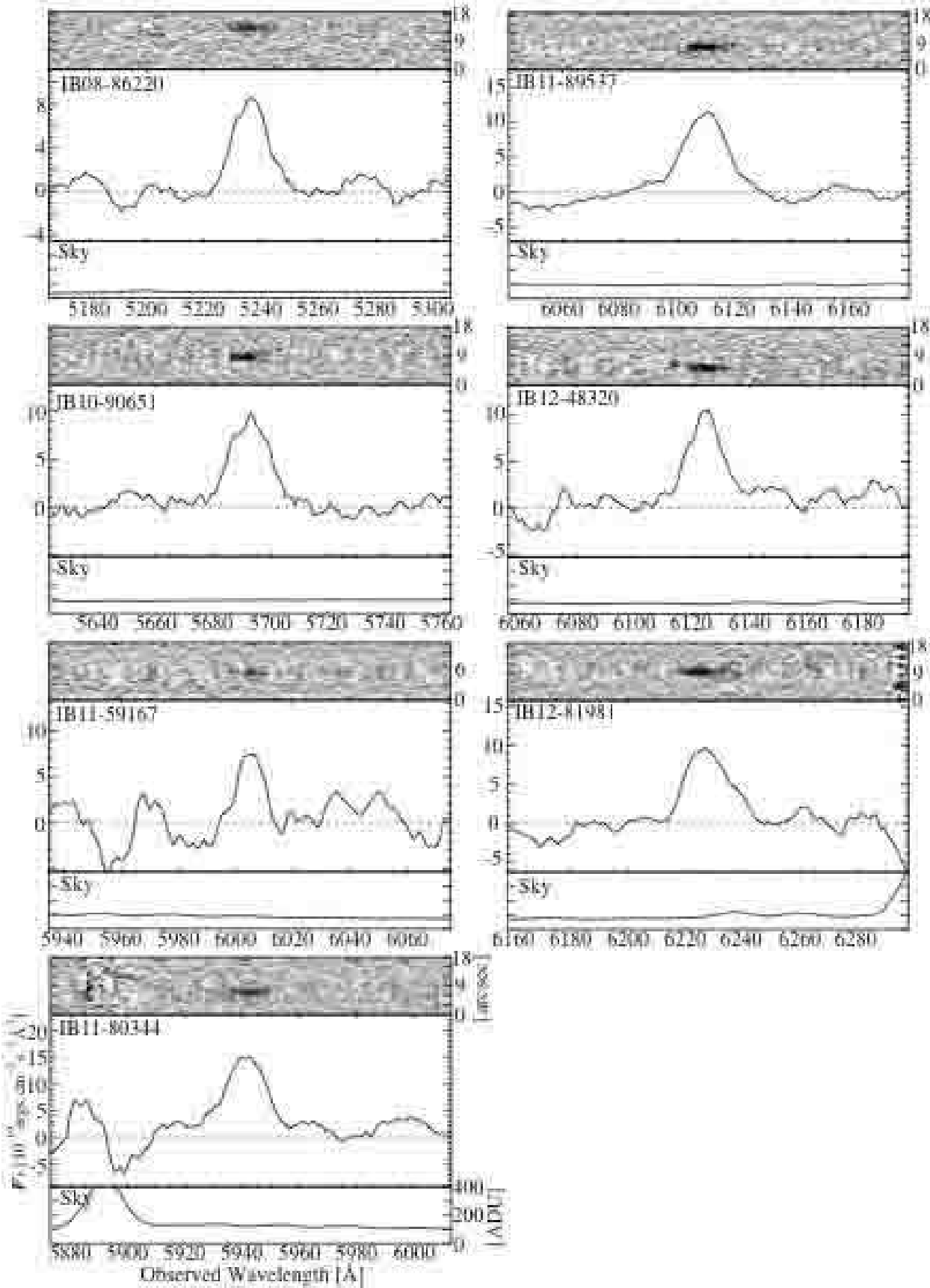


Fig. 5.— Two-dimensional and one-dimensional spectra around the Ly α emission line of the seven extended Ly α sources. The horizontal dotted lines represent the zero level. The

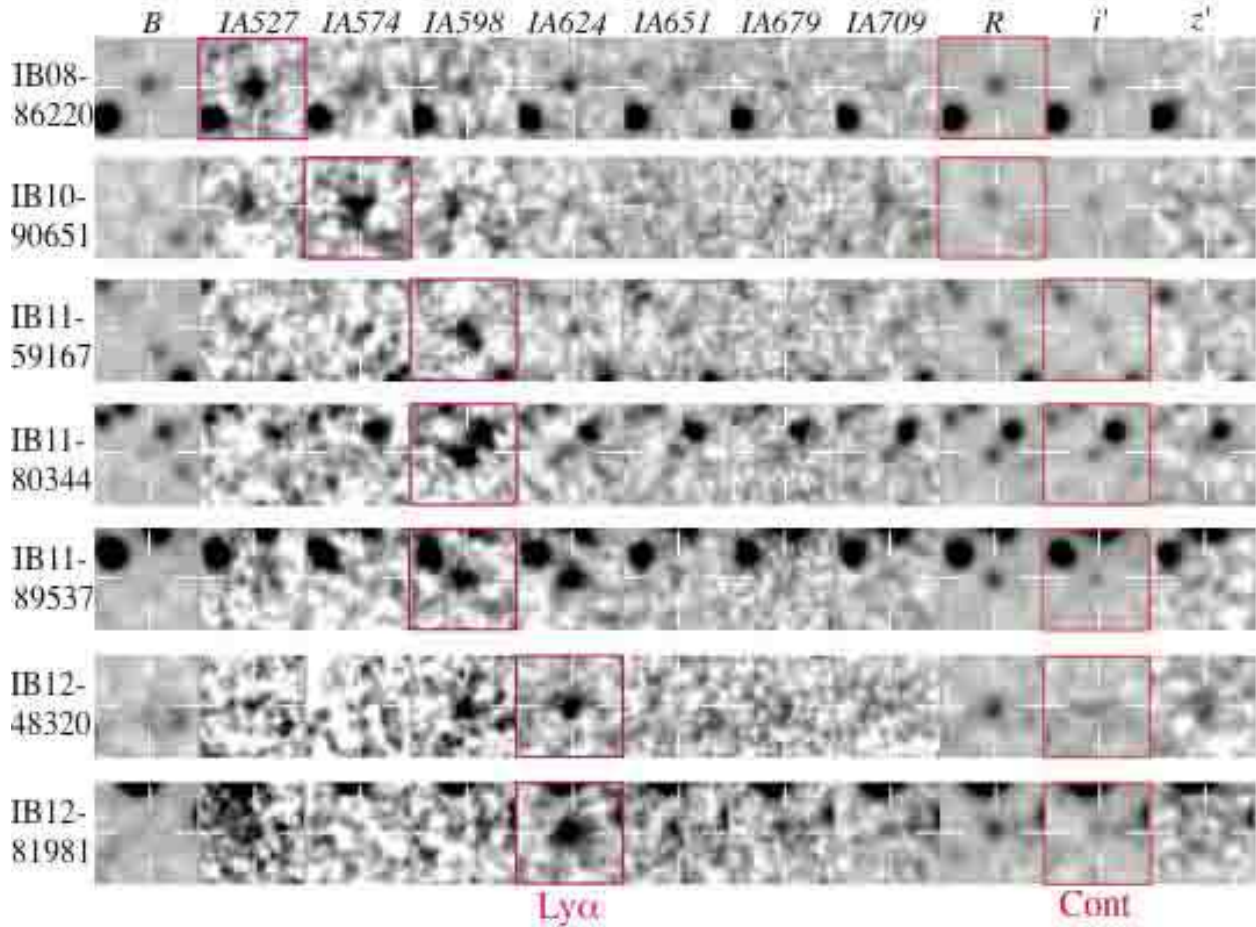


Fig. 6.— Images of the seven extended Ly α sources for which follow-up spectroscopy was made. The detected IA band images are outlined with magenta, and the broadband images used for measuring the red-ward continuum level are outlined with red color. Each image shows a region of $6'' \times 6''$.

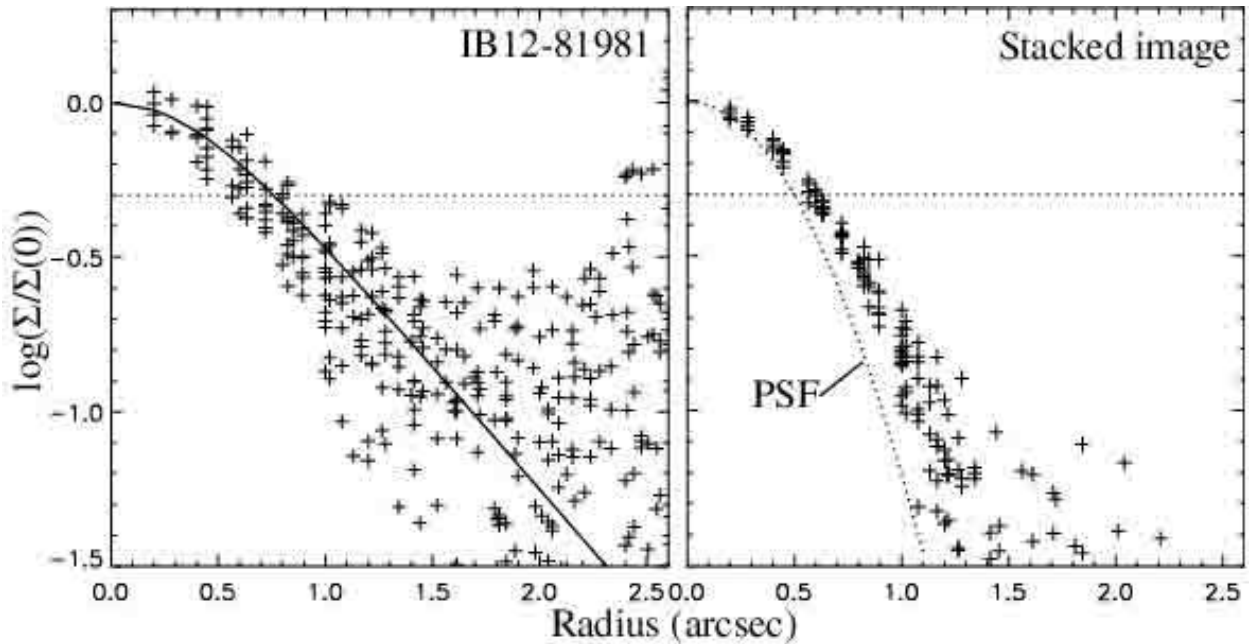


Fig. 7.— (Left) Radial surface brightness profile of IB12-81981, a typical object in our sample. Normalized surface brightness is plotted against the distance from the center of the object. The crosses show the surface brightness of each pixel, and the solid curve is the radial profile of a PSF-smoothed exponential disk with an appropriate half-light radius (HLR). (Right) Radial surface brightness profile of the stacked image of the 41 objects. The dotted curve shows the Gaussian PSF with FWHM of 1''.05. For both panels, the horizontal dotted line shows a half level of the central surface brightness.

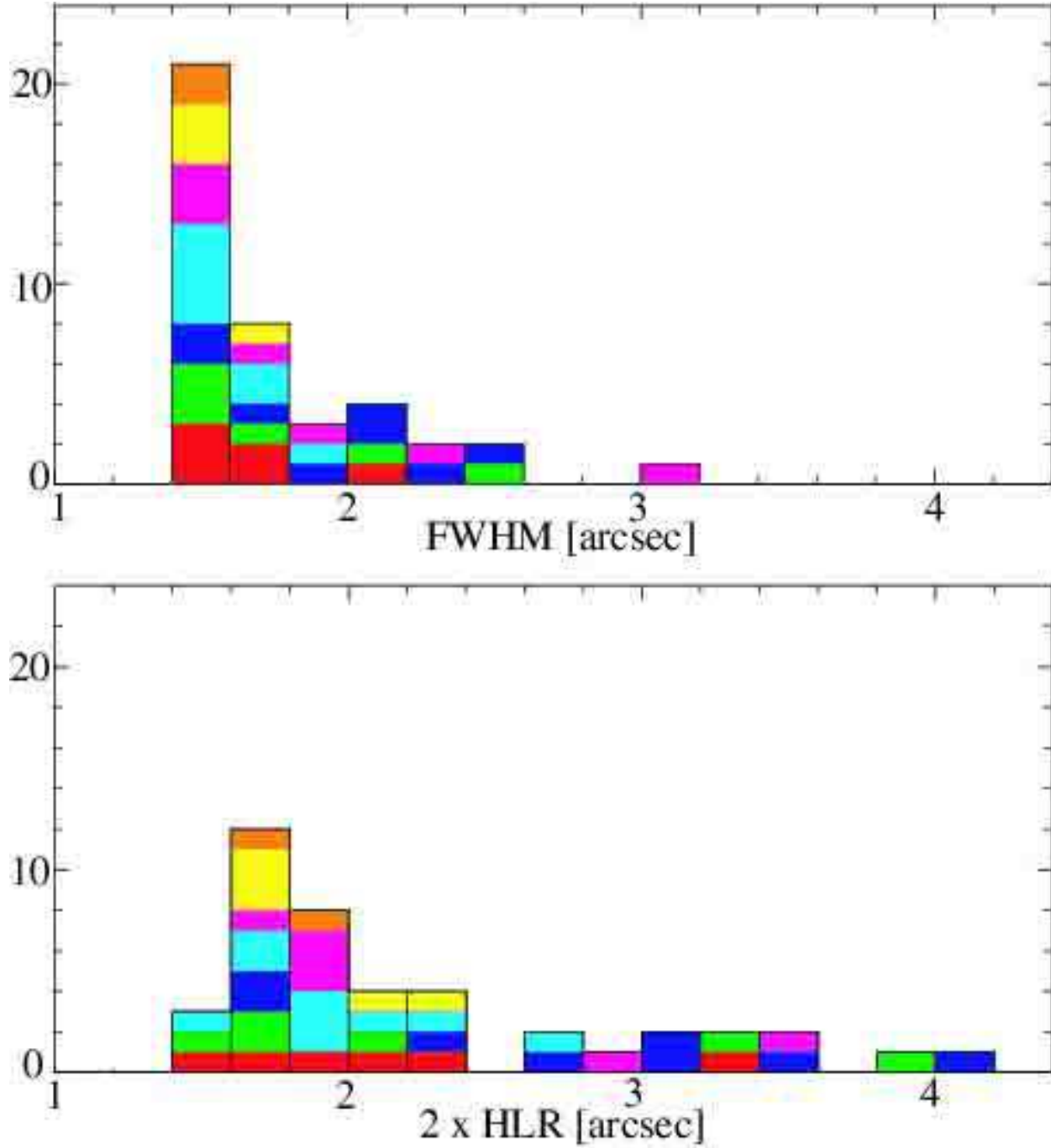


Fig. 8.— Size distribution of extended Ly α sources. The top panel is for the FWHM sizes measured on the images. The bottom panel is for the intrinsic size defined as twice the half-light-radius (HLR), calculated in our imaging simulation (see text for details). The colors show the detected IA bands: red for IA527, green for IA574, blue for IA598, cyan for IA624, magenta for IA651, yellow for IA679, and orange for IA709.

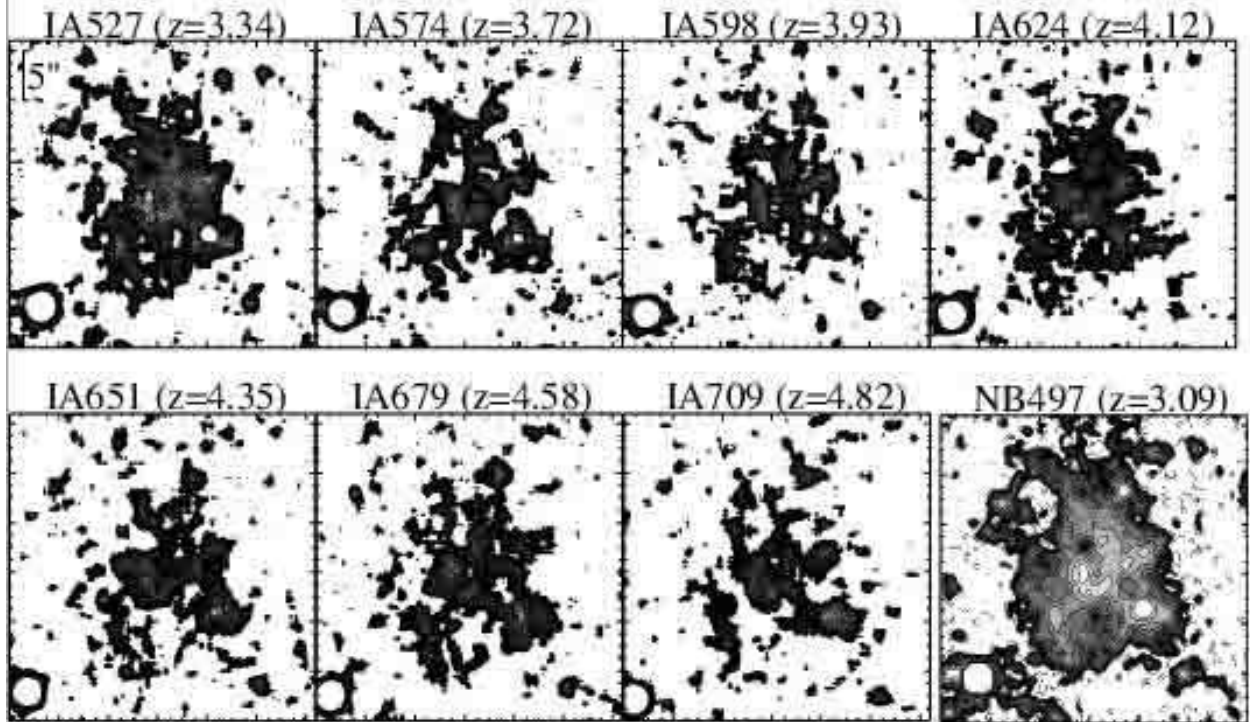


Fig. 9.— Simulated images of the LAB1 located within our redshift range and observed with our IA filters. The bottom-right panel shows the original NB497 narrowband image of the LAB1 (Matsuda: private communication). The simulated redshifts and corresponding IA bands are marked on the top of each panel. For the simulated IA images, the lowest contour represents the 2σ noise level, and the contours are marked with an interval of 1σ . For the NB497 image, the lowest contour level is 2σ , and each contour level is $\sqrt{2}$ times the previous level.

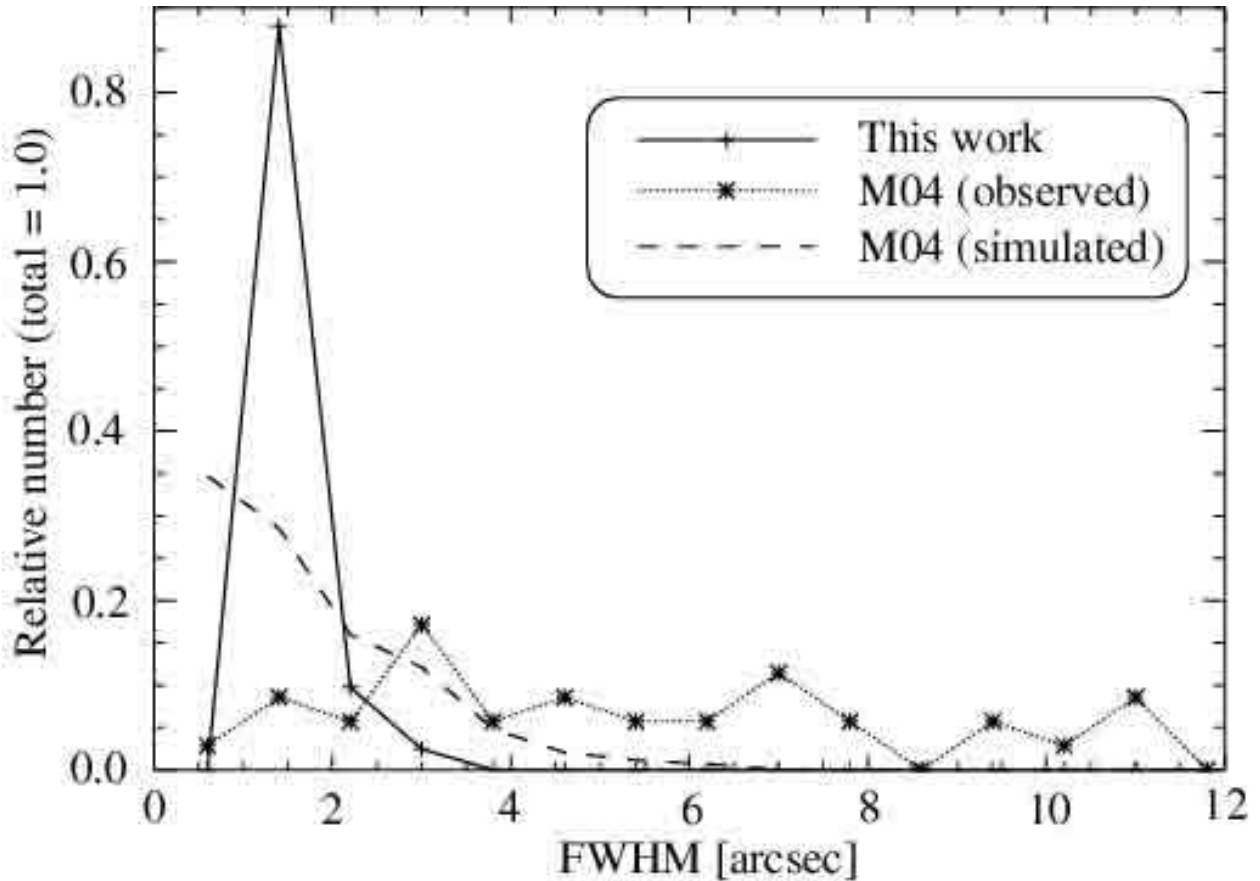


Fig. 10.— Size distributions of our sample and simulated and original M04 samples. The intermediate-band imaging simulation shown in Fig.9 was made for all the objects in M04's sample, and the sizes were measured with the same manner as for our data (see the text). The size distribution obtained in the imaging simulation is shown with the dashed line. This is the averaged distribution of the seven simulated images corresponding to the seven IA bands. The observed size distribution of our sample is shown with the solid line with crosses, and that of M04's sample is shown with the dotted line with asterisks.

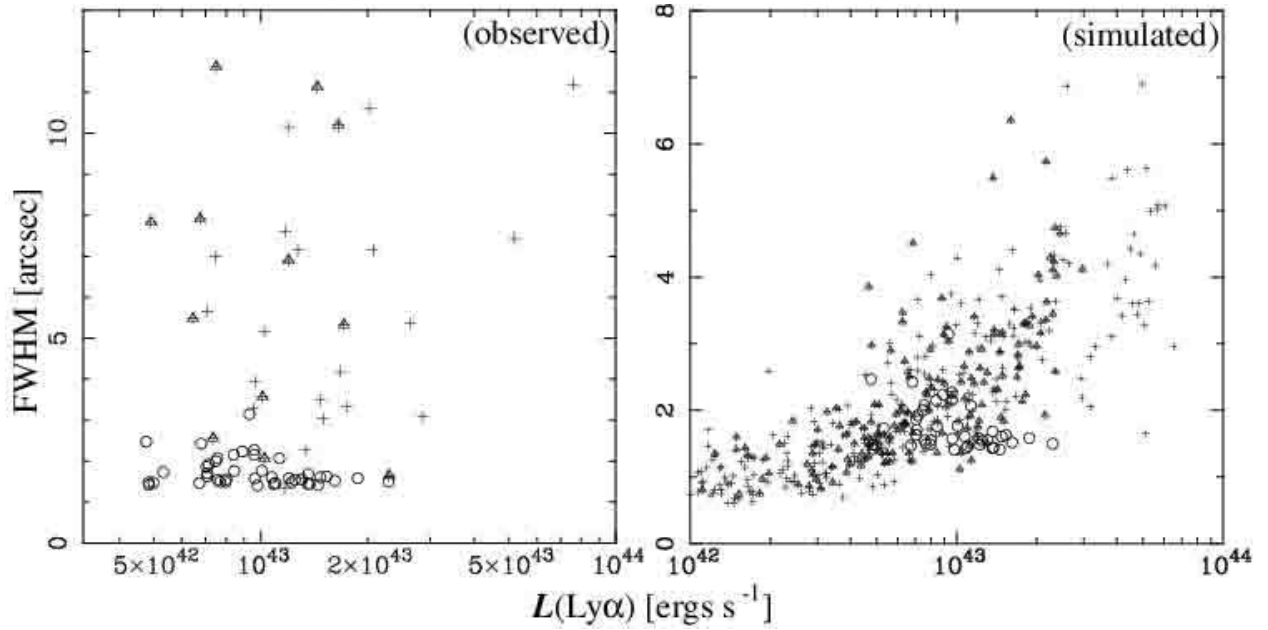


Fig. 11.— Physical sizes in FWHM plotted against Ly α line luminosity. For both panels, the open circles represent the 41 candidates in our sample. For M04’s sample, the crosses represent the all objects, and the triangles represent 12 objects which have large equivalent widths ($EW_{rest} \geq 54\text{\AA}$). The left panel shows a comparison with the M04 sample, using the original values given in M04’s catalogue. The right panel shows a comparison with the simulated M04 sample obtained with the IA imaging simulation described in §4.1.

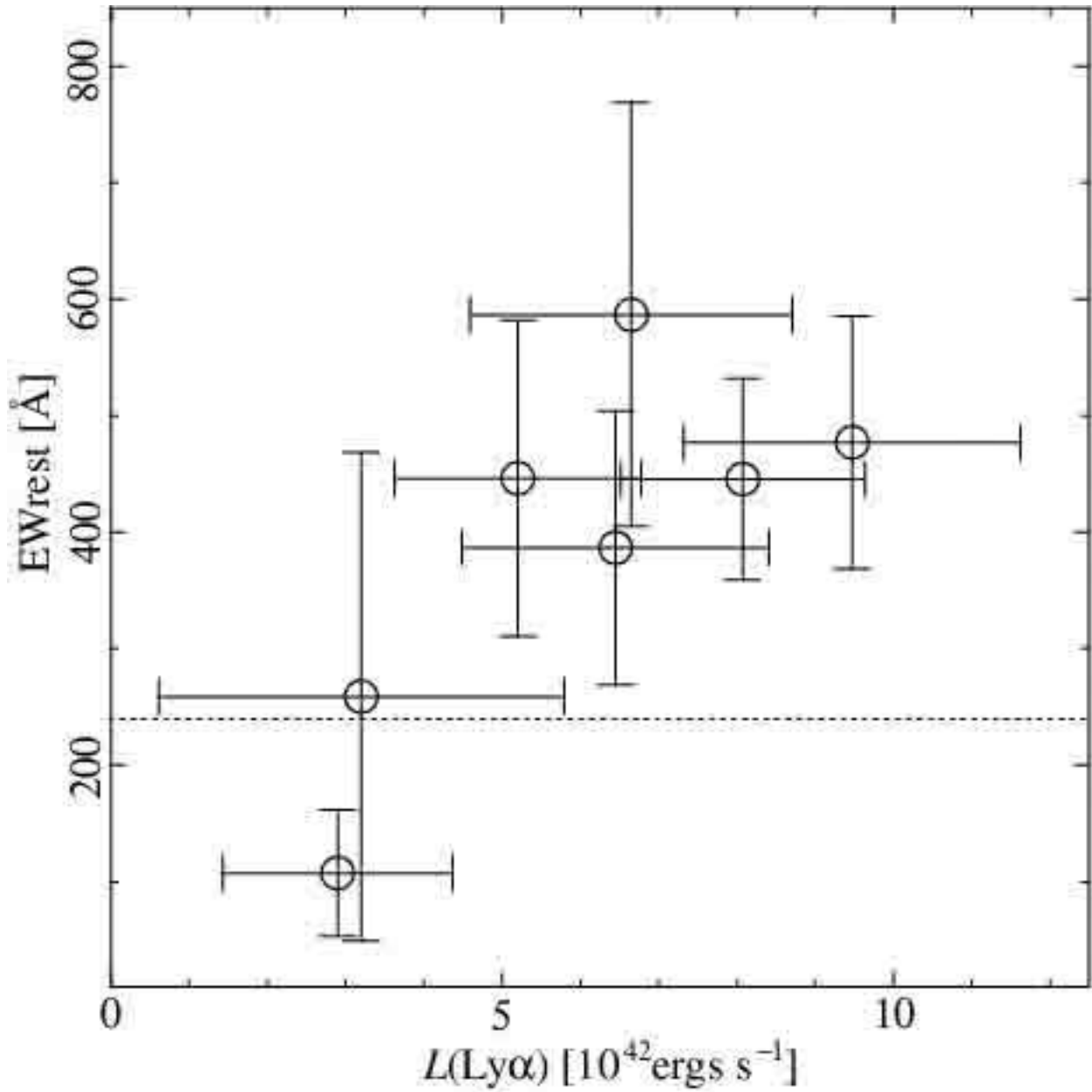


Fig. 12.— Rest-frame equivalent width of Ly α line as a function of Ly α luminosity for our spectroscopic sample. The horizontal dotted line shows 240Å, which is an upper-limit for Ly α emission of stellar origin (Malhotra & Rhoads 2002). The error bars were derived from the rms noise level of the spectral data.

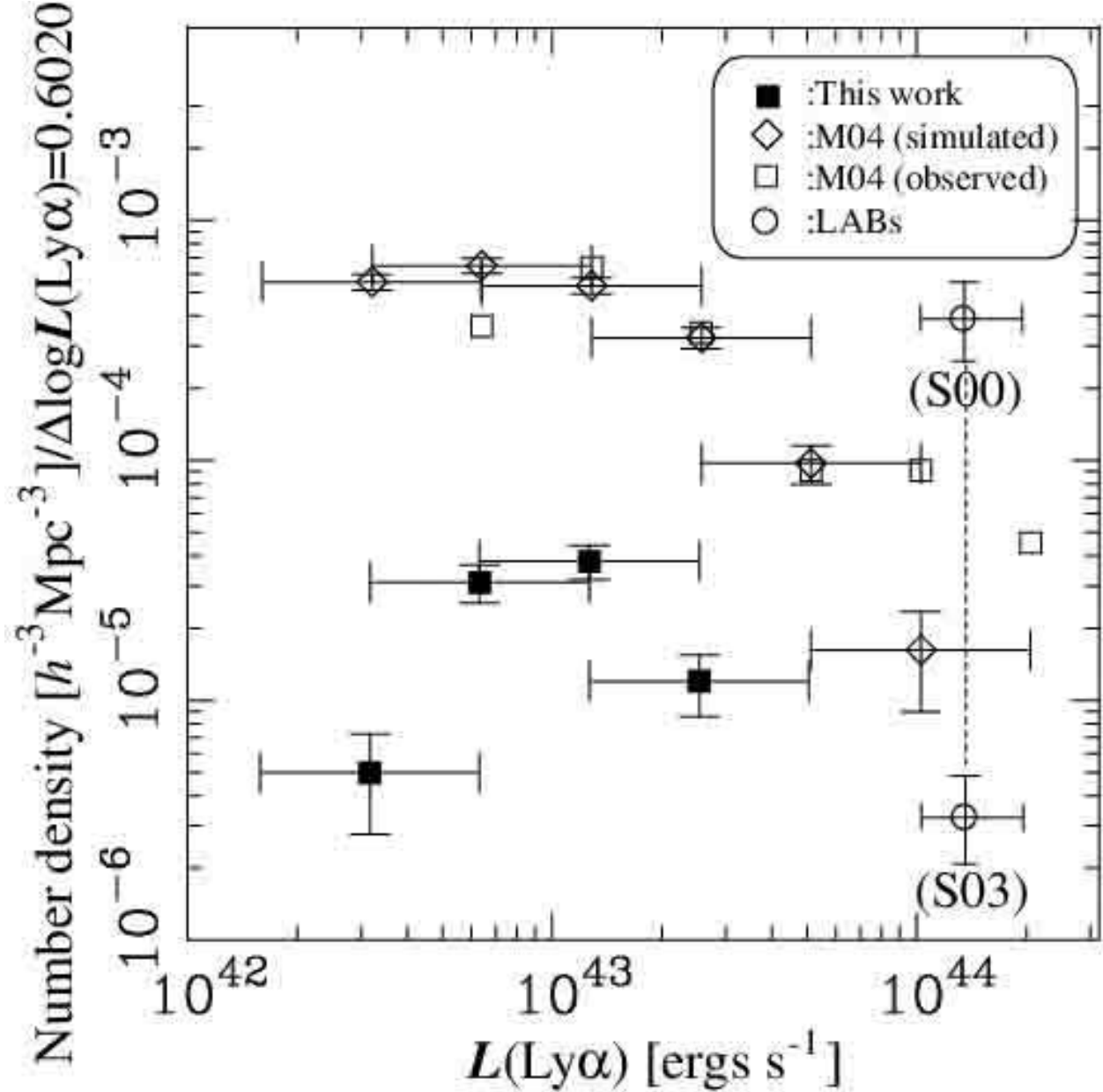


Fig. 13.— Luminosity functions (LFs) of extended Ly α sources. The filled squares show the LF of our sample. The open squares indicate the LF of M04 the sample (original values). The open diamonds are the LF of the simulated M04 sample, which was obtained with the imaging simulation described in §4.1 (see the text). The two open circles connected by the dashed line at the right end correspond to the number density of the two LABs, i.e., two divided by the survey volume of S00 (marked “(S00)”) and that of Steidel et al. (2003) (marked “(S03)”). For all the points, the horizontal error bars represent the size of the luminosity bin, and the vertical ones represent the Poisson error. No completeness correction was made for any of the points.